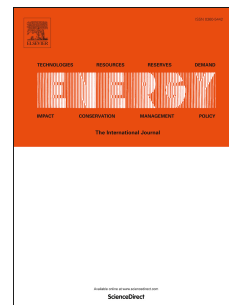


Journal Pre-proof

Numerical study on heat transfer characteristics and performance evaluation of PEMFC based on multiphase electrochemical model coupled with cooling channel

Ben Chen, Qihao Deng, Guanghua Yang, Yu Zhou, Wenshang Chen, Yonghua Cai, Zhengkai Tu



PII: S0360-5442(23)02327-7

DOI: <https://doi.org/10.1016/j.energy.2023.128933>

Reference: EGY 128933

To appear in: *Energy*

Received Date: 20 December 2022

Revised Date: 19 August 2023

Accepted Date: 27 August 2023

Please cite this article as: Chen B, Deng Q, Yang G, Zhou Y, Chen W, Cai Y, Tu Z, Numerical study on heat transfer characteristics and performance evaluation of PEMFC based on multiphase electrochemical model coupled with cooling channel, *Energy* (2023), doi: <https://doi.org/10.1016/j.energy.2023.128933>.

This is a PDF file of an article that has undergone enhancements after acceptance, such as the addition of a cover page and metadata, and formatting for readability, but it is not yet the definitive version of record. This version will undergo additional copyediting, typesetting and review before it is published in its final form, but we are providing this version to give early visibility of the article. Please note that, during the production process, errors may be discovered which could affect the content, and all legal disclaimers that apply to the journal pertain.

© 2023 Published by Elsevier Ltd.

Credit Author Statement

Author contributions:

Ben Chen: Conceptualization, Methodology, Writing Original Draft,

Qihao Deng: Conceptualization, Writing Original Draft, Software

Guanghua Yang: Resources, Writing-Review & Editing, Data Curation, Supervision

Yu Zhou: Conceptualization, Methodology, Writing Original Draft, Software

Wenshang Chen: Conceptualization, Software

Yonghua Cai: Conceptualization, Supervision

Zhengkai Tu: Resources, Writing-Review & Editing

**Numerical study on heat transfer characteristics and performance evaluation of
PEMFC based on multiphase electrochemical model coupled with cooling
channel**

Ben Chen ¹, Qihao Deng ¹, Guanghua Yang ¹, Yu Zhou ¹, Wenshang Chen ¹, Yonghua

Cai ^{1, *}, Zhengkai Tu ^{2, *}

1 Hubei Key Laboratory of Advanced Technology for Automotive Components,
Wuhan University of Technology, Wuhan, 430070, China

2 School of Energy and Power Engineering, Huazhong University of Science and
Technology, Wuhan 430074, China

* Corresponding author. E-mail:

caitrans@163.com (Y. Cai)

tzklq@hust.edu.cn (Z. Tu)

Abstract: In this study, a three-dimensional multi-phase proton exchange membrane fuel cell (PEMFC) electrochemical model coupled with a cooling channel (CC) was developed, to comprehensively analyze the heat transfer characteristics. The membrane temperature, index of uniform temperature (IUT), net power, and the Nusselt number were applied to evaluate the heat transfer performance. The results indicate that a smaller IUT value achieves better PEMFC performance at close temperatures, and the best performance is achieved with a coolant inlet temperature of 343.15 K. Although increasing the coolant flow velocity improves the cooling effect, thereby enhancing PEMFC performance. However, it inevitably leads to an increase in parasitic power, resulting in a decrease in the output power of the PEMFC system. Moreover, with the coolant temperature difference less than 6K, PEMFC shows better performance when the coolant flow direction is the same as O₂. On the contrary, with the coolant temperature difference greater than 6K, the coolant flow direction should be the same as H₂ to ensure good performance. In addition, with the temperature difference between the coolant inlet and outlet of 10K, 6K, and 3K, respectively, the surface Nusselt number of wavy CC is 5.46%, 8.92%, and 18.71% higher than the straight CC, respectively.

Keywords: PEMFC; Heat transfer; Cooling channel; IUT; Nusselt number

1 Introduction

Hydrogen energy has been widely recognized as one of the most promising clean energy sources [1]. The Proton exchange membrane fuel cell (PEMFC) uses hydrogen as fuel, and the reaction process produces virtually no other impurities, and the only by-products are water and heat [2]. Due to the outstanding advantages of high efficiency, high power density, rapid start-up speed, low operating temperature, and zero pollution [3, 4], PEMFC is considered a most promising candidate energy conversion device for transportation, standby, fixed and portable application, and has even been used in submarines and aerial vehicles [5, 6]. PEMFC applications focus on transportation as a primary domain, with significant attention currently focused on proton exchange membrane fuel cell vehicles (PEMFCVs), such as passenger vehicles, commercial vehicles, and buses.

Generally, the power of PEMFCVs ranges from 20 to 250 kW to meet the requirements of different applications [7]. Due to the fact that PEMFC is not limited by the Carnot cycle, its energy conversion efficiency reaches 40%~60%, and almost all remaining energy is converted into heat [8]. This is due to a large amount of heat generated by ohmic resistance, mass transfer overpotential, and irreversibility of electrochemical reactions during their operation [9, 10]. The regular operation of PEMFC is greatly affected by the operating temperature [11]. The proton exchange membrane can be destroyed by excessive temperature, while low temperature can cause a slow reaction [12]. Therefore, efficient and appropriate cooling enables PEMFC to obtain higher power, safe operation and long working life [13]. Maintaining uniform temperature

inside the PEMFC is another crucial aspect of PEMFC thermal management. Performance degradation can easily be caused by an uneven temperature distribution inside the PEMFC [14, 15]. Reasonable cooling design enables PEMFC to operate at expected temperatures, thereby stimulating the performance potential of PEMFC [16]. Currently, PEMFC cooling methods include air cooling, phase change cooling, heat radiators, and liquid cooling [17, 18]. Although the air-cooling PEMFC dramatically reduces the cost and simplifies the system [19], it suffers from a severe dependence on ambient temperature and a lack of active cooling capacity [20]. PEMFC stacks with heat radiators for cooling have received a lot of attention [21], and various studies have developed ultra-thin vapor chambers as heat pipes [22, 23]. Phase change cooling with the outstanding advantages of low coolant velocity and straightforward system design. The expensive expense of phase change materials, however, has prevented phase change cooling from being widely used in PEMFC stacks [21]. Liquid cooling is typically used for high-power PEMFC stacks above 5 kW due to its high cooling efficiency and cooling performance [18, 24]. With the widespread use of liquid cooling in PEMFC thermal management, scholars have extensively researched cooling flow fields, coolants, radiators, and strategies for improving cooling performance [20]. Convection between the coolant and the bipolar plate is almost the only way to carry away the heat generated in PEMFC through liquid cooling [25]. Reasonable cooling flow field and coolant velocity can ensure uniform temperature distribution of PEMFC, and operate at the optimal operating temperature.

There have been numerous experimental research on the thermal and water

management of liquid-cooled PEMFCs [26, 27]. Visual experiments and infrared thermography were used to explore the hydrothermal distribution of PEMFC. In addition, Al_2O_3 nanofluids [28], ZnO nanofluids [29], and micro-encapsulated phase change suspensions [30] have been used as coolants for PEMFC, and all of them outperformed water in terms of cooling performance. However, the transfer phenomena involved in water and thermal management in PEMFC are complex and interact, including charge transport, multicomponent gas transport, two-phase flow, and heat transfer in different components, et al. [31]. It is challenging to gather comprehensive water and heat data by in-situ measurements due to the intense interaction of these processes and the compactness of PEMFC. In contrast, Computational Fluid Dynamics (CFD) simulations are more suitable for analyzing the water and heat transfer process and the interaction between water and heat in PEMFC[17].

The structures and types of the cooling flow field have a considerable impact on the flow characteristics and heat transfer effectiveness of the coolant. Baek et al. [32] designed six different structures of cooling flow fields and performed non-isothermal model simulation without electrochemistry. They considered that flow field design has a significant influence on temperature distribution. Chen et al. [33] designed MIMO-type cooling flow fields with different inlet and outlet directions and evaluated their cooling performance through an index of uniform temperature (IUT). They found that the cooling performance was best when the inlet and outlet directions were opposite. Zhang et al. [34, 35] constructed a metallic PEMFC structure with a wavy flow field. They demonstrated that the flow field temperature distribution was more uniform when

the cooling flow field was in the same direction as the cathode. Alizadeh et al. [36] designed an effective cooling flow field and studied the effects of laminar and turbulent flow on heat transfer and pressure difference. Deng et al. [37] evaluated four cooling flow fields. The results showed that the pressure difference of the serpentine cooling flow field increased sharply with the increase of coolant velocity, and the wave cooling flow field performed well. Afshari et al. [38, 39] built a zigzag cooling flow field and found that the pressure difference of the serpentine cooling flow field was substantial. The cooling performance of metal foam and zigzag cooling flow field was qualified with a lower pressure difference. Song et al. [40] found that the multi-channel cooling flow field performed better by designing six different cooling flow fields. Yu et al. [41] improved the serpentine flow field to obtain a better cooling effect and more minor pressure difference, but the influence of pressure difference can't be ignored. Vazifeshenas et al. [42] found that adding metal foam into the cooling flow field was useful but accompanied by high-pressure difference. In addition, they found that water performed better than glycol as a coolant. Li et al. [43,44] established a three-dimensional cooling channel model for research and analysis, the conventional straight channel, wave channel, and novel non-uniform channel have all been constructed. Their findings indicate that the new channel design greatly improves cooling performance. In the investigations mentioned above, the CFD models of various cooling flow fields were developed. The numerical simulation was used to assess the cooling effects of various cooling flow fields, which provides guidance for cooling flow field design. These computational calculations, however, do not account for the electrochemical

reaction and mass transfer of PEMFC.

In some studies, electrochemical models of PEMFC with a cooling flow field have been developed to study the heat transfer characteristics. Rahgoshay et al. [45] applied the serpentine cooling flow field to PEMFC and found that it improved the uniformity of the temperature distribution on the proton exchange membrane significantly. Sasmito et al. [46] investigated the impacts of PEMFC stack cooling channel design. They discovered that serpentine cooling flow fields provided the optimum cooling and PEMFC stack performance. However, traditional serpentine designs perform poorly due to excessive pressure differences and parasitic loads. Penga et al. [47] proposed a flow field with coolant-induced variable temperature, where high relative humidity can be maintained by the coolant temperature. Liu et al. [48] established a three-dimensional straight channel PEMFC model with a coolant channel. They investigated how the performance of PEMFC was impacted by coolant velocity, inlet temperature, coolant direction, and the number of cooling channels. They believed pursuing very high-temperature uniformity along the passage direction was unnecessary. The temperature distribution along the channel should be carefully designed by adjusting the coolant velocity. Atyabi et al. [49, 50] designed five different cooling flow field structures for electrochemical performance research, including metal foam flow field and heat pipe cooling, and the results showed that heat pipe obtained lower IUT. Furthermore, they also proposed a comprehensive three-dimensional multiphase PEMFC model with a novel flow field pattern at the cathode side, which was used for the reference design of the cooling flow field [51, 52]. The results indicate that

embedding a separate cooling channel can enhance cooling and stabilize proton transport on the membrane. Ghasemi et al. [53] established six various kinds of cooling flow fields, including spiral flow fields, quantified and calculated the parasitic power generated by the pumped coolant, and more carefully considered the impact of the coolant pressure difference on the comprehensive performance of PEMFC. Liu et al. [54] studied the influence of the coolant flow direction and demonstrated that PEMFC performed best when the coolant flow direction was the same as the cathode gas. Wang et al. [55] established an electrochemical model of PEMFC with cooling surfaces. The results reveal that the current density and peak power density dropped as the temperature difference between the cooling surfaces grew.

Although numerous cooling flow fields were constructed to increase PEMFC performance in previous studies, only the heat transfer properties of the cooling flow field were simulated, and most designs neglected the electrochemical model. The heat generated by the electrochemical reaction is assumed a continuous and homogeneous heat flux, which is not the practice case. Furthermore, when developing the PEMFC electrochemical simulation model, some studies ignored the modeling of the cooling flow fields, setting the wall surface of the PEMFC to equal temperature, thereby ignoring the effect of the cooling flow field on the electrochemical properties of the PEMFC and the internal water heat distribution, which are relatively imperfect places. Therefore, a PEMFC electrochemical model integrating the cooling channel is established in this study, and the effects of the cooling channel (CC) structure, temperature, flow velocity, and flow direction on PEMFC performance and water heat

distribution are analyzed in detail. The study proposes a wave CC design for PEMFC that enhances heat transfer capability, improves temperature distribution uniformity, and prevents liquid water collection, consequently enhancing the electrochemical properties of PEMFC. Furthermore, the heat transfer superiority of wave CC is evaluated by various evaluation indicators, such as the IUT, the net power, and the Nusselt number. The results of this research are expected to provide practical guidance for optimizing the heat transfer performance of PEMFC and enhancing its performance, safety, and working life.

2 Geometry Model

The three-dimensional PEMFC model is developed, as shown in Fig.1. The active area is $2.2 \text{ mm} \times 100 \text{ mm}$.

Two types of CC are designed, which are the straight CC and wave CC, and their xOz plane schematic is shown in Fig. 2. The wave CC is represented by:

$$Z = A \sin(Bx) + C \quad (1)$$

$$T = \frac{2\pi}{B} \quad (2)$$

where T represents the period.

Additionally, Table 1 shows the related single cell physical parameters.

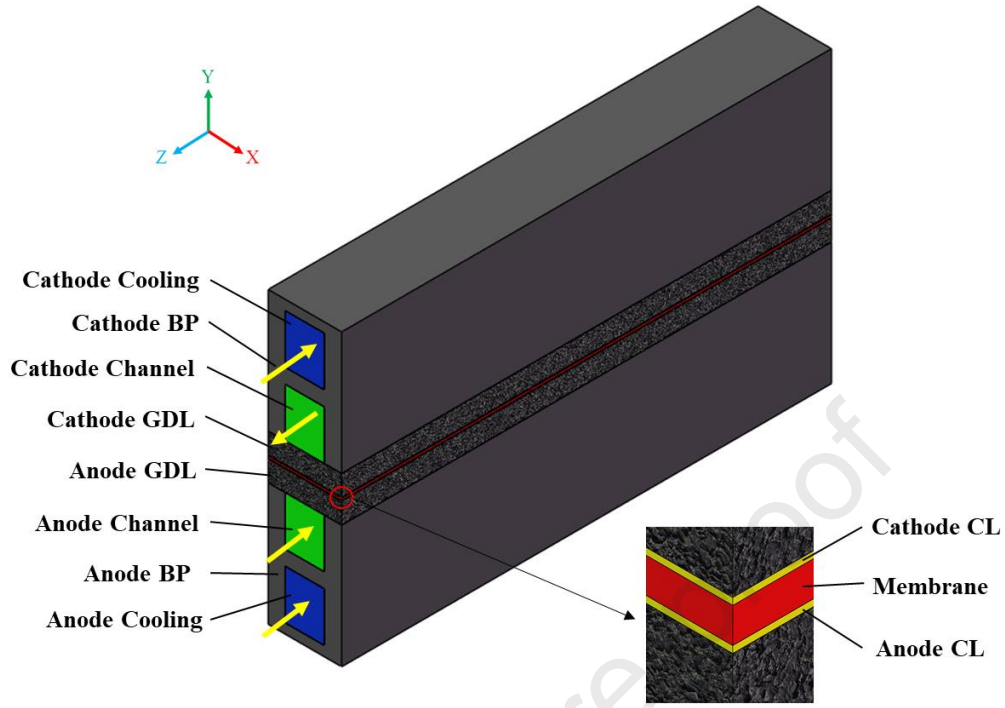


Figure 1. The structure of a single cell with CCs

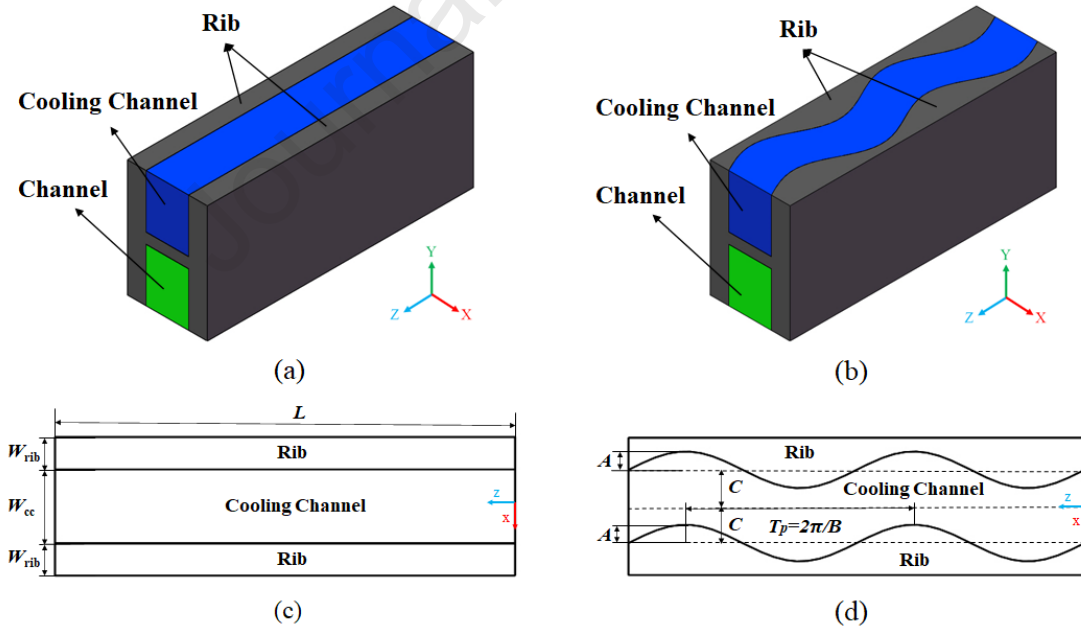


Figure 2 Schematic three-dimensional models of (a) straight CC (b) wave CC, and details of dimension and geometrics of (c) straight CC (d) wave CC

Table 1 Geometric and physical parameters [56, 57].

Parameters	Symbol	Straight	Wave
Diffusion layer thickness (μm)	δ_{GDL}	420	420
Catalyst layer thickness (μm)	δ_{CL}	10	10
MEM thickness (μm)	δ_{mem}	50.8	50.8
Channel width, height, length (mm)	$W_{\text{ch}}, H_{\text{ch}}, L_{\text{ch}}$	0.8, 1.0, 100	0.8, 1.0, 100
CC width, height, length (mm)	$W_{\text{cc}}, H_{\text{cc}}, L_{\text{cc}}$	0.8, 1.0, 100	0.8, 1.0, 100
Rib width (mm)	W_{rib}	0.7	/
Amplitude of the sine wave	A	/	0.2
Coefficient for determining the period of a sine function	B	/	0.4π
Position of the sine wave reference line in the direction of X	C	/	0.4
Intrinsic permeability of GDL, CL, MEM (m^2)	$K_{\text{GDL}}, K_{\text{CL}},$	$8.76 \times 10^{-13}, 10^{-13},$	$8.76 \times 10^{-13}, 10^{-13},$
	K_{mem}	2.0×10^{-20}	2.0×10^{-20}
Electronic conductivity of GDL, CL, BP ($\text{S} \cdot \text{m}^{-1}$)	$\kappa_{\text{GDL}}, \kappa_{\text{CL}}, \kappa_{\text{BP}}$	4000, 2000,	4000, 2000,
		20,000	20,000
Thermal conductivity of GDL, CL, MEM, BP ($\text{W} \cdot \text{m}^{-1} \cdot \text{K}^{-1}$)	$k_{\text{GDL}}, k_{\text{CL}},$	1.0, 1.0, 0.95, 20.0	1.0, 0.95, 20.0
	$k_{\text{mem}}, k_{\text{BP}}$		
Ionomer volume fraction	ω	0.27	0.27

3 Numerical model

3.1 Model assumptions

Reasonable model assumptions simplify calculations and reduce calculation time, and the model assumptions are as follows [54, 57]:

- (1) Both gas flow and coolant flow are incompressible and laminar flow;
- (2) All gases are considered ideal gases;

(3) Gas diffusion follows Fick's Law of Binary Diffusion;

(4) The PEMFC operates at a steady state.

3.2 Conservation equations

The mass conservation equation of the gas mixture is as follows (solved in Channel, GDL, and CL):

$$\nabla \cdot (\rho_g \vec{u}_g) = S_g \quad (3)$$

where ρ_g is the density of gas, \vec{u}_g is the velocity of gas, S_g is the quality source term.

That of coolant is as follows (solved in CC):

$$\nabla (\rho_w \cdot \vec{u}_w) = 0 \quad (4)$$

Where ρ_w is the coolant density, \vec{u}_w is the coolant velocity vector.

The momentum conservation equation of the gas mixture is as follows (solved in, Channel, GDL, and CL):

$$\nabla \cdot \left(\frac{\rho_g \vec{u}_g \vec{u}_g}{\varepsilon^2} \right) = -\nabla P_g + \mu_g \nabla \cdot (\nabla \vec{u}_g) + S_u \quad (5)$$

Where ε is material porosity; P_g is gas pressure; μ_g is the dynamic viscosity of gas; S_u is the momentum source term.

That of coolant is as follows (solved in CC):

$$\nabla \cdot (\rho_w \vec{u}_w \vec{u}_w) = -\nabla P_w + \mu_w \nabla \cdot (\nabla \vec{u}_w) \quad (6)$$

where P_w is coolant pressure; μ_w is coolant dynamic viscosity;

The gas species transport conservation equation is as follows (solved in Channel, GDL, CL):

$$\nabla \cdot (\rho_g \vec{u}_g Y_i) = \nabla \cdot (\rho_g D_i^{\text{eff}} \nabla Y_i) + S_i \quad (7)$$

where Y_i is the mass fraction; D_i^{eff} is the effective diffusion coefficient; S_i is the mass

source term; subscript i represents different gases.

Dissolved water as follows (solved in CL, MEM):

$$\nabla \cdot \left(\frac{2.5}{22F} I_{\text{ion}} \lambda \right) = \frac{\rho_{\text{mem}}}{EW} \nabla \cdot (D_{\text{d}}^{\text{eff}} \nabla \lambda) + S_{\text{mw}} \quad (8)$$

where I_{ion} is ionic current density, ρ_{mem} is dry film density of MEM, λ is membrane water content, EW is equivalent mass of membrane, $D_{\text{d}}^{\text{eff}}$ is effective dissolved water diffusivity, S_{mw} is membrane water source term, F is Faraday constant.

The energy conservation equation is as follows (all):

$$\nabla \cdot (\rho_w C_{p,w} \vec{u}_w T + \varepsilon s \rho_l C_{p,l} \vec{u}_l T + \varepsilon (1-s) \rho_g C_{p,g} \vec{u}_g T) = \nabla \cdot (k_e^{\text{eff}} \nabla T) + S_T \quad (9)$$

Where k_e^{eff} is effective thermal conductivity, s is the liquid water saturation, C_p is the constant pressure specific heat, T is temperature, S_T is the thermal source term.

Liquid water volume fraction as follows (solved in channel):

$$\nabla \cdot (\rho_l \vec{u}_l s) = 0 \quad (10)$$

Where the \vec{u}_l is the liquid water velocity, ρ_l is the liquid water density.

Liquid pressure is as follows (solved in GDL, CL):

$$0 = \nabla \cdot \left(\rho_l \frac{K k_l}{\mu_l} \nabla P_l \right) + S_l \quad (11)$$

where P_l is liquid pressure, μ_l is the dynamic viscosity of liquid, K is the intrinsic permeability, k_l is the liquid phase relative permeability, S_l is the liquid pressure source term.

The capillary pressure P_c is defined as follows:

$$P_c = P_g - P_l \quad (12)$$

Where P_g , P_l is the gas pressure and the liquid pressure, respectively.

The liquid water saturation (s) are as follows:

$$P_c = \sigma |\cos \theta| \left(\frac{\varepsilon}{K} \right)^{0.5} J(s) \quad (13)$$

$$J(s) = 1.417s - 2.12s^2 + 1.263s^3 \quad (14)$$

Where σ is the surface tension coefficient, θ is the contact angle.

3.3 Electrochemistry models

The governing equations for the electrical charge of electron and proton can be written as follows:

$$0 = \nabla \cdot (\kappa_{\text{sol}} \nabla \varphi_{\text{sol}}) + S_{\text{sol}} \quad (15)$$

$$0 = \nabla \cdot (\kappa_{\text{mem}} \nabla \varphi_{\text{mem}}) + S_{\text{mem}} \quad (16)$$

where κ_{sol} and κ_{mem} are the electrical conductivity of solid and MEM; φ_{sol} and φ_{mem} are the phase potential of solid and MEM; S_{sol} and S_{mem} are the volume exchange current density of solid and MEM.

The MEM electrical conductivity κ_{mem} is determined by an empirical correlation as follows:

$$\kappa_{\text{mem}} = (0.514\lambda - 0.326) \exp \left(1268 \left(\frac{1}{303} - \frac{1}{T} \right) \right) \quad (17)$$

The electrochemical reaction rates are given by the Butler-Volmer equation:

$$J_a = J_{0,a}^{\text{ref}} \left(\frac{[A]}{[A]_{\text{ref}}} \right)^{0.5} \left(\exp \left(\frac{2\alpha_{\text{an}}^{\text{an}} F \eta_{\text{an}}}{RT} \right) - \exp \left(\frac{2\alpha_{\text{cat}}^{\text{an}} F \eta_{\text{an}}}{RT} \right) \right) \quad (18)$$

$$J_c = J_{0,c}^{\text{ref}} \left(\frac{[C]}{[C]_{\text{ref}}} \right)^2 \left(-\exp \left(\frac{4\alpha_{\text{an}}^{\text{cat}} F \eta_{\text{cat}}}{RT} \right) + \exp \left(\frac{4\alpha_{\text{cat}}^{\text{cat}} F \eta_{\text{cat}}}{RT} \right) \right) \quad (19)$$

where η is the activation over-potential, J_a and J_c represents anode and cathode exchange current density, $J_{0,a}^{\text{ref}}$ and $J_{0,c}^{\text{ref}}$ represents anode and cathode reference

current density; $[A]$ and $[C]$ represent the molar concentration of H_2 and O_2 ; α represents the charge transfer coefficient, R is the universal gas constant.

η_{an} and η_{cat} are defined as: φ_{sol} and φ_{mem} as follows:

$$\eta_{an} = \varphi_{sol} - \varphi_{mem} \quad (20)$$

$$\eta_{cat} = E_{rev} - \varphi_{sol} + \varphi_{mem} \quad (21)$$

Where E_{rev} represents the reversible thermodynamic cell voltage, given by the Nernst equation:

$$E_{rev} = 1.229 - 0.9 \times 10^{-3} (T - 298.15) + \frac{RT}{2F} (\ln P_{H_2}^{in} + 0.5 \ln P_{O_2}^{in}) \quad (22)$$

Where P^{in} is the partial pressure.

The main Model parameters are shown in Table 2, the main Transport properties in this study are presented in Table 3, and the Source terms are given in Table 4.

Table 2 Model parameters[56, 57]

Parameters	Symbol	Value
Density of MEM ($kg \cdot m^{-3}$)	ρ_{mem}	1980
Equivalent weight of ionomer ($kg \cdot mol^{-1}$)	EW	1.1
Faraday's constant ($C \cdot mol^{-1}$)	F	96487.0
Universal gas constant ($J \cdot mol^{-1} \cdot K^{-1}$)	R	8.314
Anode entropy change ($J \cdot mol^{-1} \cdot K^{-1}$)	ΔS_a	130.68
Cathode entropy change ($J \cdot mol^{-1} \cdot K^{-1}$)	ΔS_c	32.55
Condensation rate constant for water (s^{-1})	γ_{cond}	5000.0
Evaporation rate constant for water (s^{-1})	γ_{evap}	10^{-4}
Latent heat coefficient ($J \cdot mol^{-1}$)	h	44900.0
Anode reference exchange current density ($A \cdot m^{-3}$)	$J_{0,a}^{ref}$	1×10^8

Cathode reference exchange current density ($\text{A}\cdot\text{m}^{-3}$)	$J_{0,c}^{\text{ref}}$	120
reference hydrogen concentration ($\text{mol}\cdot\text{m}^{-3}$)	$C_{\text{H}_2}^{\text{ref}}$	56.4
reference oxygen concentration ($\text{mol}\cdot\text{m}^{-3}$)	$C_{\text{O}_2}^{\text{ref}}$	3.39
Anode transfer coefficient	α_a	0.5
Cathode transfer coefficient	α_c	0.5
liquid water surface tension ($\text{N}\cdot\text{m}^{-1}$)	σ	0.0625

Table 3 Transport properties[56]

Parameters	Expressions
Gas mixture density ($\text{kg}\cdot\text{m}^{-3}$)	$\rho_g = p_g \left(RT \sum_i \frac{Y_i}{M_i} \right)^{-1}$
Dynamic viscosity of gas mixture ($\text{kg}\cdot\text{m}^{-1}\cdot\text{s}^{-1}$)	$\mu_g = \sum_i \frac{X_i \mu_i}{\sum_j X_j \phi_{ij}}$
Hydrogen diffusivity ($\text{m}^2\cdot\text{s}^{-1}$)	$D_{\text{H}_2} = 1.005 \times 10^{-4} \left(\frac{T}{333.15} \right)^{1.5} \left(\frac{101325}{P} \right)$
Oxygen diffusivity ($\text{m}^2\cdot\text{s}^{-1}$)	$D_{\text{O}_2} = 2.652 \times 10^{-5} \left(\frac{T}{333.15} \right)^{1.5} \left(\frac{101325}{P} \right)$
Water vapor diffusivity in anode ($\text{m}^2\cdot\text{s}^{-1}$)	$D_v^a = 1.005 \times 10^{-4} \left(\frac{T}{333.15} \right)^{1.5} \left(\frac{101325}{P} \right)$
Water vapor diffusivity in cathode ($\text{m}^2\cdot\text{s}^{-1}$)	$D_v^c = 2.982 \times 10^{-5} \left(\frac{T}{333.15} \right)^{1.5} \left(\frac{101325}{P} \right)$
Gas effective diffusivity ($\text{m}^2\cdot\text{s}^{-1}$)	$D_i^{\text{eff}} = (1-s)^{1.5} \varepsilon^{1.5} D_i$
Dynamic viscosity of liquid water ($\text{kg}\cdot\text{m}^{-1}\cdot\text{s}^{-1}$)	$\mu_l = 2.414 \times 10^{\frac{247.8}{T-140}}$
Gas phase and liquid phase relative permeability (m^2)	$k_g = (1-s)^3, k_l = s^3$

Saturation pressure (pa)	$\log_{10} \frac{P_{\text{sat}}}{101325} = -2.1794 + 0.02953(T - 273.15) - 9.1837 \times 10^{-5} (T - 273.15)^2 + 1.4454 \times 10^{-7} (T - 273.15)^3$
Phase change between vapor and liquid water ($\text{kg} \cdot \text{m}^{-3} \cdot \text{s}^{-1}$)	$S_{v-l} = \begin{cases} \gamma_{\text{cond}} \varepsilon (1-s) \frac{(P_v - P_{\text{sat}})}{RT} & P_v > P_{\text{sat}} \\ \gamma_{\text{evap}} \varepsilon s \frac{(P_v - P_{\text{sat}})}{RT} & P_v < P_{\text{sat}} \end{cases}$
Phase change between dissolved water and liquid water ($\text{kg} \cdot \text{m}^{-3} \cdot \text{s}^{-1}$)	$S_{d-v} = 1.3 \frac{\rho_{\text{mem}}}{EW} (\lambda - \lambda_{\text{eq}}) M_{\text{H}_2\text{O}}$
MEM water content	$\lambda = \frac{EW}{\rho_{\text{mem}}} C_{\text{H}_2\text{O}}$
Dissolved water diffusivity ($\text{m}^2 \cdot \text{s}^{-1}$)	$D_d^{\text{eff}} = \begin{cases} 3.1 \times 10^{-7} \lambda (e^{0.28\lambda} - 1) e^{\frac{-2346}{T}} & 0 < \lambda < 3 \\ 4.17 \times 10^{-8} \lambda (161e^{-\lambda} + 1) e^{\frac{-2346}{T}} & 3 \leq \lambda \leq 17 \\ 4.1 \times 10^{-10} \left(\frac{\lambda}{25}\right)^{0.15} \left(1 + \tan\left(\frac{\lambda - 2.5}{1.4}\right)\right) & \lambda > 17 \end{cases}$
Water activity	$a = \frac{P_v}{P_{\text{sat}}} + 2s$
Equilibrium MEM water content	$\lambda_{\text{eq}} = \begin{cases} 0.043 + 17.84a - 39.85a^2 + 36a^3 & 0 \leq a \leq 1 \\ 14 + 14(a - 1) & 1 < a \leq 3 \end{cases}$

Table 4 Source terms of conservation equations[56].

Source terms	units
$S_g = \begin{cases} 0 & \text{Channels} \\ -S_{v-l} & \text{GDLs} \\ -S_{v-l} + S_{d-v} - \frac{J_a}{2F} M_{\text{H}_2} & \text{Anode CL} \\ -S_{v-l} + S_{d-v} - \frac{J_c}{4F} M_{\text{O}_2} & \text{Cathode CL} \end{cases}$	$\text{kg} \cdot \text{m}^{-3} \cdot \text{s}^{-1}$
$S_u = \begin{cases} 0 & \text{Channels} \\ -\frac{\mu_g}{Kk_g} \bar{u}_g & \text{GDLs, CLs} \end{cases}$	$\text{kg} \cdot \text{m}^{-2} \cdot \text{s}^{-2}$

$$S_{H_2} = \begin{cases} -\frac{J_a}{2F} M_{H_2} & \text{Anode CL} \\ 0 & \text{Channels, GDLs, Cathode CL} \end{cases} \quad \text{kg} \cdot \text{m}^{-3} \cdot \text{s}^{-1}$$

$$S_{O_2} = \begin{cases} -\frac{J_c}{4F} M_{O_2} & \text{Cathode CL} \\ 0 & \text{Channels, GDLs, Anode CL} \end{cases} \quad \text{kg} \cdot \text{m}^{-3} \cdot \text{s}^{-1}$$

$$S_v = \begin{cases} 0 & \text{Channels} \\ -S_{v-l} & \text{GDLs} \\ -S_{v-l} + S_{d-v} & \text{Anode CL} \\ -S_{v-l} + S_{d-v} - \frac{J_c}{2F} M_{H_2O} & \text{Cathode CL} \end{cases} \quad \text{kg} \cdot \text{m}^{-3} \cdot \text{s}^{-1}$$

$$S_l = -S_{v-l} \quad \text{GDLs, CLs} \quad \text{kg} \cdot \text{m}^{-3} \cdot \text{s}^{-1}$$

$$S_{mw} = \begin{cases} 0 & \text{Membrane} \\ -S_{d-v} - \rho_l \frac{K_{mem} (P_1^{ACL} - P_1^{CCL})}{\mu_l \delta_{mem} \delta_{CL}} & \text{Anode CL} \\ -S_{d-v} + \rho_l \frac{K_{mem} (P_1^{ACL} - P_1^{CCL})}{\mu_l \delta_{mem} \delta_{CL}} & \text{Cathode CL} \end{cases} \quad \text{kg} \cdot \text{m}^{-3} \cdot \text{s}^{-1}$$

$$S_{sol} = \begin{cases} -J_a & \text{Anode CL} \\ J_c & \text{Cathode CL} \end{cases} \quad \text{A} \cdot \text{m}^{-3}$$

$$S_{mem} = \begin{cases} J_a & \text{Anode CL} \\ -J_c & \text{Cathode CL} \end{cases} \quad \text{A} \cdot \text{m}^{-3}$$

$$S_T = \begin{cases} \|\nabla \varphi_e\|^2 \kappa_e^{eff} & \text{BPs} \\ 0 & \text{Channels} \\ 0 & \text{CCs} \\ \|\nabla \varphi_e\|^2 \kappa_e^{eff} + hS_{v-l} & \text{GDLs} \\ \|\nabla \varphi_e\|^2 \kappa_e^{eff} + \|\nabla \varphi_e\|^2 \kappa_{ion}^{eff} + hS_{v-l} - hS_{d-v} + J_a |\eta_a| + \frac{J_a T \Delta S_a}{2F} & \text{Anode CL} \\ \|\nabla \varphi_e\|^2 \kappa_e^{eff} + \|\nabla \varphi_e\|^2 \kappa_{ion}^{eff} + hS_{v-l} - hS_{d-v} + J_c |\eta_c| + \frac{J_c T \Delta S_c}{4F} & \text{Cathode CL} \\ \|\nabla \varphi_{ion}\|^2 \kappa_{ion}^{eff} & \text{Membrane} \end{cases} \quad \text{W} \cdot \text{m}^{-3}$$

3.4 Boundary conditions

Anode and cathode inlet boundary conditions are mass flow inlet boundary, the inlet mass flow rate (\dot{m}_a and \dot{m}_c) as follows [56]:

$$\dot{m}_a = \frac{I^{ref} \rho_g^a \xi_a A}{2F c_{H_2}}; \dot{m}_c = \frac{I^{ref} \rho_g^c \xi_c A}{2F c_{O_2}} \quad (23)$$

Where I^{ref} is the reference current density, A is the active area, ρ_g^a and ρ_g^c is the densities mixture gas at anode or cathode, ξ_a and ξ_c is the stoichiometric ratio at anode and cathode.

c_{H_2} is the hydrogen molar concentration and c_{O_2} is the oxygen molar concentration as follows:

$$c_{H_2} = \frac{P_g^a - RH_a P^{sat}}{RT}; c_{O_2} = \frac{0.21(P_g^c - RH_c P^{sat})}{RT} \quad (24)$$

where P^{sat} is the saturation pressure, P_g^a and P_g^c is the inlet pressure; RH_a and RH_c is the relative humidity. Table 5 shows the main operating parameters.

The coolant flow is calculated as follows [37]:

$$Q_c = \frac{nqA}{\Delta T C_{p,c} \rho_c} \quad (25)$$

The coolant velocity is calculated as follows:

$$V_{in} = \frac{Q_c}{A_{in}} \quad (26)$$

Q_c stands for the coolant flow, n is the number of single cells, q stands for the exothermic power density, A stands for the active area, ΔT stands for the coolant temperature difference between inlet and outlet (Hereinafter collectively referred to as coolant temperature difference), $C_{p,c}$ stands for the constant pressure heat capacity of coolant, ρ_c stands for the coolant density, V_{in} stands for the coolant inlet velocity, A_{in} stands for the coolant inlet area. Table 6 shows different numerical cases.

Table 5 Operating parameter of PEMFC [56, 57]

Parameters	Symbol	Experiment	Simulation
Anode inlet temperature (K)	T_a	353.15	353.15
Cathode inlet temperature (K)	T_c	353.15	353.15
Anode operating pressure (Pa)	P_a	101315	101315
Cathode operating pressure (Pa)	P_c	101315	101315
Anode stoichiometric ratio	ξ_a	2.0	2.0
Cathode stoichiometric ratio	ξ_c	1.5	1.5
Reference current density ($A \cdot m^{-2}$)	I^{ref}	NA	10,000
Anode inlet relative humidity	RH_a	84%	84%
Cathode inlet relative humidity	RH_c	59%	59%

Table 6 Numerical cases

	ΔT (K)	CC pattern
Case A	10	straight
Case B	10	wave
Case C	6	straight
Case D	6	wave
Case E	3	straight
Case F	3	wave

3.5 Mesh independence and model validation

The precision of the calculations in the numerical simulation increases with the number of grids. [58]. In this study, straight CC models with the following grid numbers have been established for verification: 13750, 22000, 35200, 50800, 72160, 112000, 209000,

332000, and 531000. The chosen current density is 1 A/cm^2 , and the variation in voltage, the maximum temperature, and pressure difference with the number of grids measured at 1 A/cm^2 are shown in Fig. 3. In this study, the working voltage of the fuel cell tends to stabilize after the grid number is more than or equal to 209000, hence the model with a grid number of 209000 is utilized for numerical simulation.

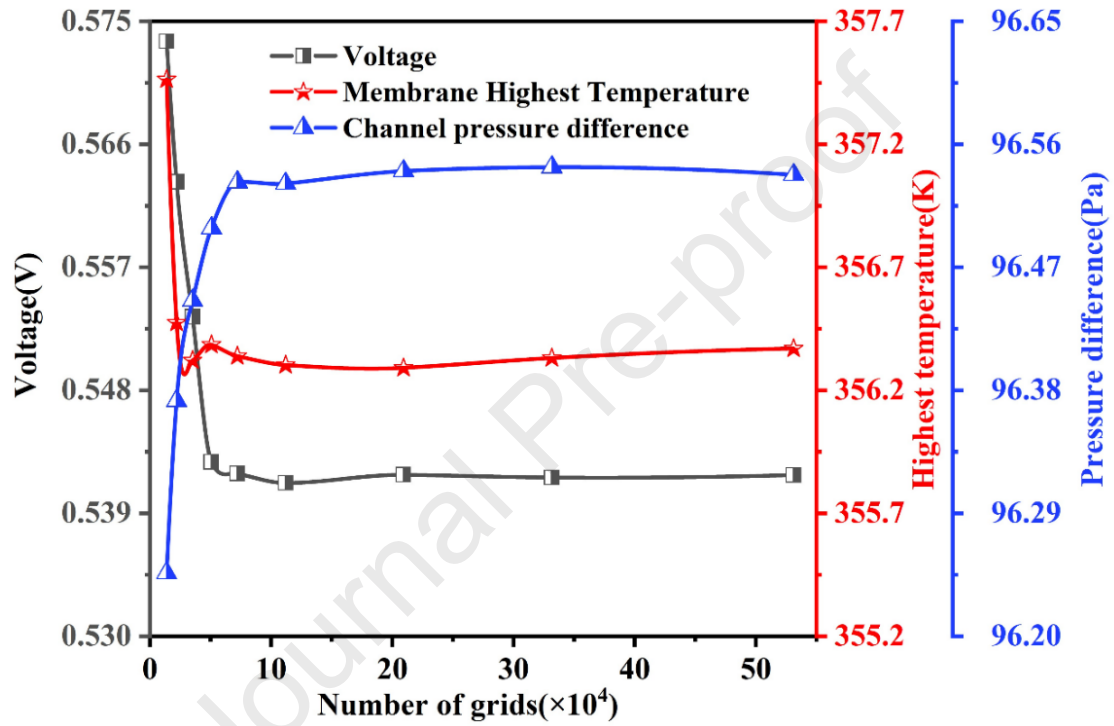


Figure 3 Mesh independence verification

The model for validation is calculated without coolant flow. The wall temperature of the two plates is set to 353.15K. By comparison with the experimental results[57], which are shown in Fig.4, the differences of each point are less than 1%, and it is considered that the results of this numerical model are reliable.

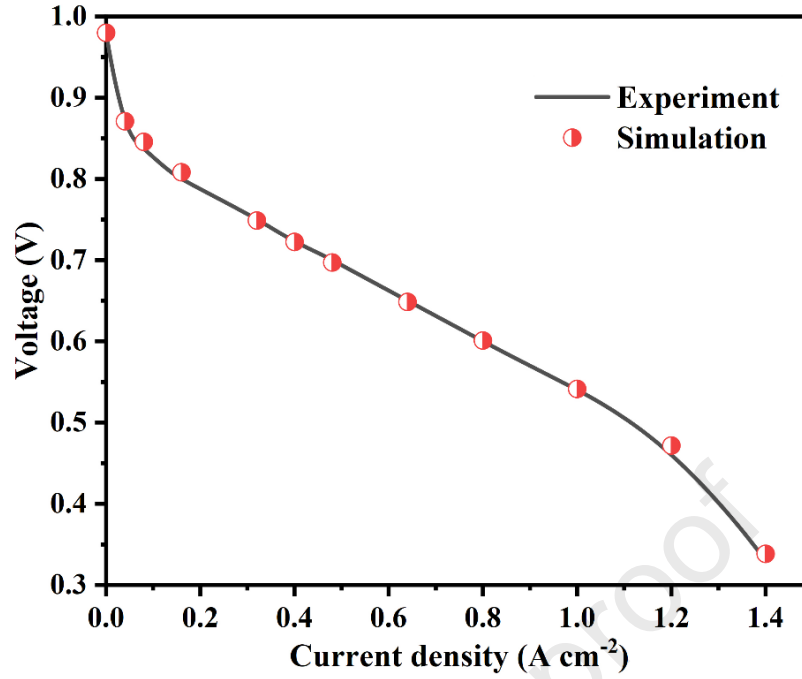


Figure 4 Comparison between the polarization of simulation and experimental

4 Results and discussion

This section evaluates the effects of coolant inlet temperature, coolant flow direction, coolant velocity, and CC structure on PEMFC performance, respectively. The cooling performance has been analyzed by the IUT in MEM, and the heat transfer performance of CCs is evaluated by the surface Nusselt number. The boundary conditions for operation are shown in Table 5, and Formulas 25 and 26. The coolant velocities are set as constants in boundary condition settings. In practice, the coolant velocity varies with the voltage of the PEMFC, which is controlled by setting the coolant temperature difference to ensure proper cooling of PEMFC under different voltages. The unspecified coolant flow directions in this study are all in the same direction as the anode (H_2).

4.1 Effect of cooling water inlet temperature

Fig. 5(a) shows the current density from Case A to Case F at different coolant

temperatures with a voltage of 0.46V and ΔT of 10K, 6K, and 3K, respectively. It is found that the PEMFC performs best at a coolant inlet temperature of 343.15K with a ΔT of 3K. Additionally, at a coolant inlet temperature of 338.15K with a ΔT of 10K, the PEMFC performs slightly poorer. The wavy CC can achieve a higher current density than the straight channel at the same inlet temperature and ΔT .

The average temperature and IUT on the MEM from Case A to Case F are shown in Fig. 5(b).

The IUT is calculated as follows [41]:

$$IUT = \frac{\int_v |T - T_{avg}| dV}{\int_v dV} \quad (27)$$

Where:

$$T_{avg} = \frac{\int_v T dV}{\int_v dV} \quad (28)$$

Where T_{avg} represents the average temperature. The smaller IUT, the more uniform the temperature distribution.

As shown in Fig. 5(b), it is found that the PEMFC achieved the best performance at the average temperature of MEM is close to 350K in this electrochemical model. Case B, Case D and Case F perform optimally at coolant inlet temperatures of 338.15K, 340.65K and 343.15K respectively, the average temperature on MEM is close to 350K at these conditions. Due to the reaction gas temperature being 353.15K, the lower the temperature of the coolant, the more significant the temperature difference between the coolant and PEMFC, which can lead to an uneven uniformity of temperature

distribution on the membrane. Fig. 5(b) shows that the lower the coolant inlet temperature, the higher the IUT value, and the more uneven the temperature distribution. Furthermore, Case E and Case F show the smallest IUT, and Case A and Case B show the largest IUT, indicating that coolant velocity greatly affects the membrane temperature distribution. In summary, the temperature distribution on the MEM greatly affects the performance of the PEMFC, and it performs best at the average temperature of MEM is close to 350K, the coolant inlet temperature at this condition is 343.15K. That is, the average MEM temperature is the primary factor affecting PEMFC performance, and the performance of PEMFC is improved by a smaller IUT at the average MEM temperature is close.

Fig. 6 shows the temperature distribution on the MEM for Case B, Case D, and Case F at various coolant inlet temperatures. The comparison shows that, for a given coolant velocity, a higher coolant input temperature corresponds to a higher MEM temperature. The coolant velocity also significantly affected the MEM temperature distribution and PEMFC performance, especially the impact on the maximum temperature for MEM, and it is discussed in later sections. According to the results of the above analysis, both Case E and Case F achieve the best performance at the coolant inlet temperature of 343.15K, which indicate this model performs best at a coolant inlet temperature of 343.15K. Therefore, the coolant inlet temperature of 343.15K is used in the following studies to investigate the optimal performance of the model.

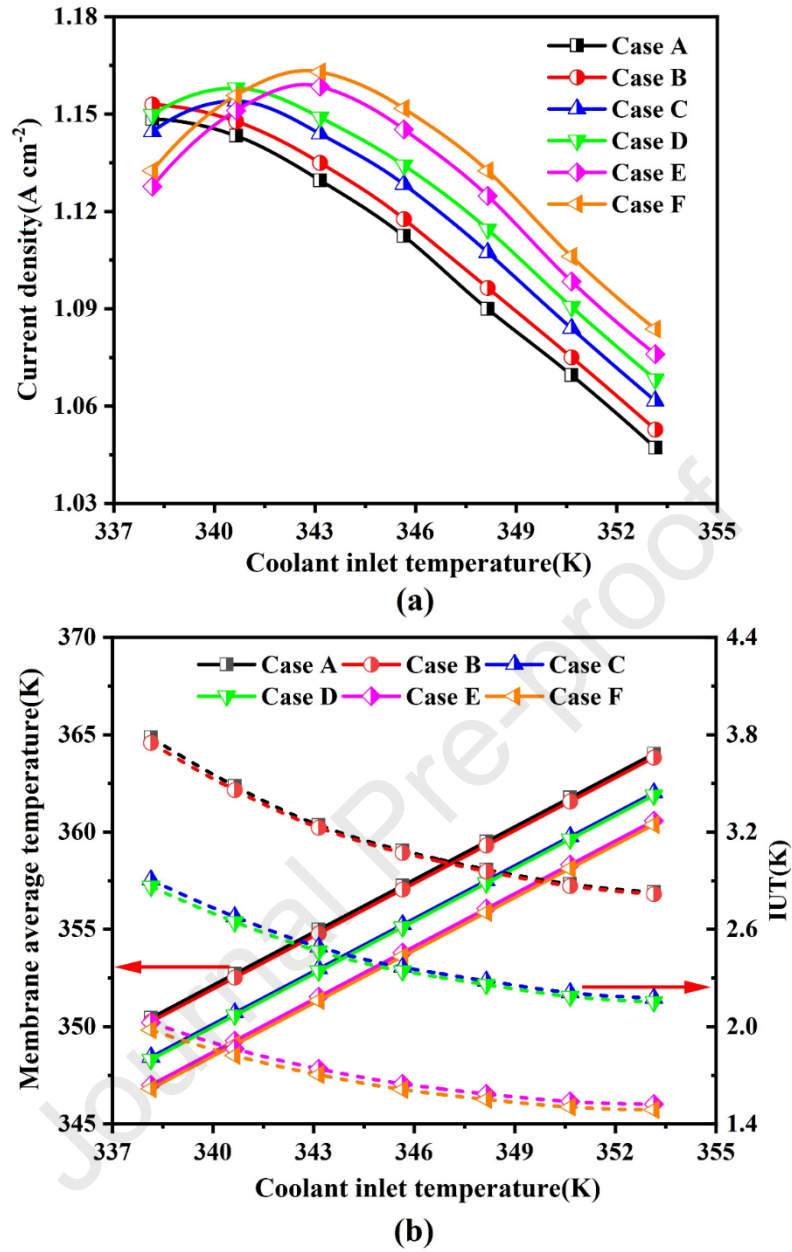


Figure 5 Effect of coolant inlet temperature on (a): current density; (b): The average temperature and IUT on the MEM

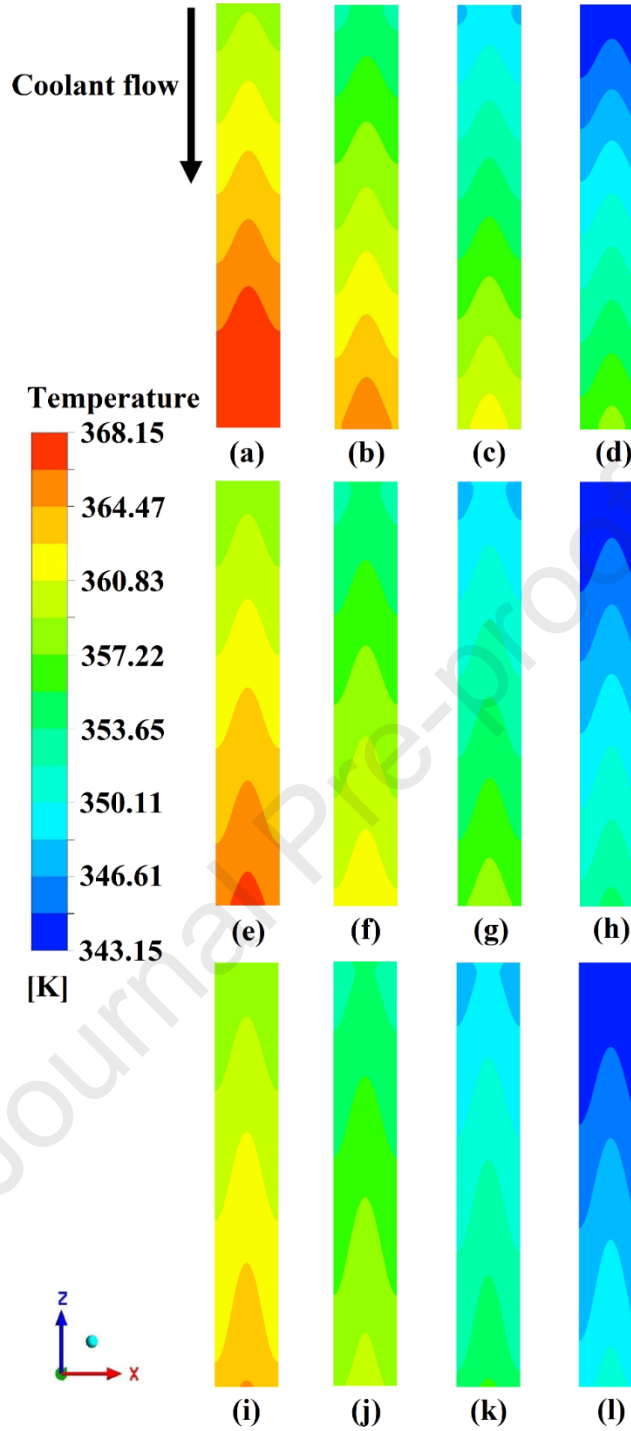


Figure 6 Temperature distribution on MEM at different coolant inlet temperatures. (a) (b) (c) (d): Case B with coolant inlet temperature of 353.15K, 348.15K, 343.15K, 338.15K, respectively; (e) (f) (g) (h): Case D with coolant inlet temperature of 353.15K, 348.15K, 343.15K, 338.15K, respectively; (i) (j) (k) (l): Case F with coolant inlet temperature of 353.15K, 348.15K, 343.15K, 338.15K, respectively.

4.2 Effect of coolant flow velocity

The net power calculation formula is shown below [53, 59]:

$$P_{net} = P_{gross} - P_{para} \quad (29)$$

$$P_{gross} = V_{cell} jA \quad (30)$$

The parasitic power is the power consumption caused by factors such as water pumps in PEMFC. The calculation formula of the parasitic power dissipation is:

$$P_{para} = \frac{\Delta P Q_c}{\eta_{pump}} \quad (31)$$

P_{net} is net power density; P_{gross} is total output power; P_{para} is the parasitic power by the pressure difference of CC; V_{cell} is the PEMFC voltage; j is the average current density; A is the active area; ΔP is the pressure difference; Q_c is coolant flow; η_{pump} is the efficiency of pump.

In the previous section, the coolant velocity is determined by Equations 25 and 26, where the coolant velocity is determined by the coolant temperature difference and is inversely proportional under the same working condition. In this section, the coolant inlet temperature is set to 343.15K, and the coolant flow direction is the same as H₂. Fig. 7 shows the polarization and net power density curves from Case A to Case F, and Fig. 7 (b) is an enlarged view of the last three points in Fig. 7 (a). The polarization and the net power density curves achieve the maximum difference at 0.46V. The current density from Cases A to Case F is 1.130 A/cm², 1.137 A/cm², 1.146 A/cm², 1.153 A/cm², 1.156 A/cm² and 1.163 A/cm², respectively. However, the current density difference becomes smaller from Case A to Case F at 0.33V, the current density from Case A to Case F is 1.347 A/cm², 1.355 A/cm², 1.352 A/cm², 1.360 A/cm², 1.356 A/cm² and 1.364

A/cm^2 , respectively. This indicates that since the lower temperature prevents liquid water to be discharged, the accumulation of liquid water causes mass transfer losses and leads the concentration polarization, which has a significant negative impact on the performance of PEMFC.

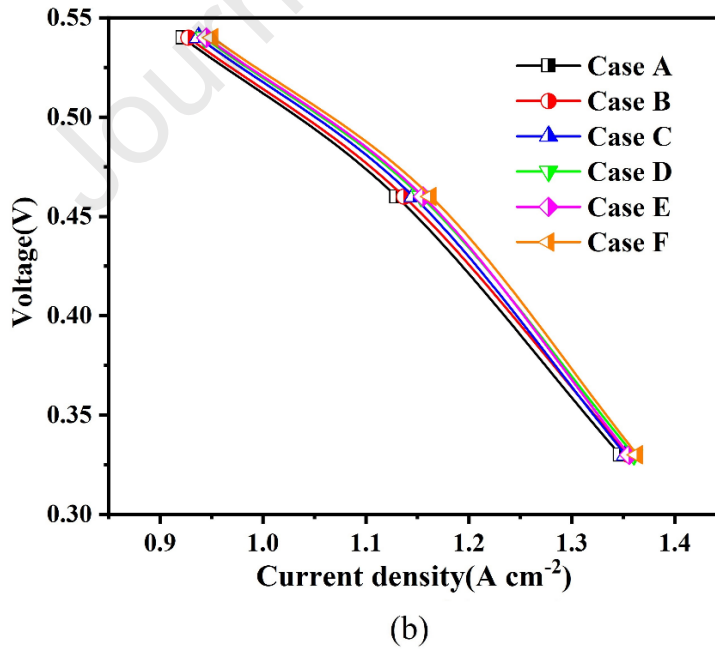
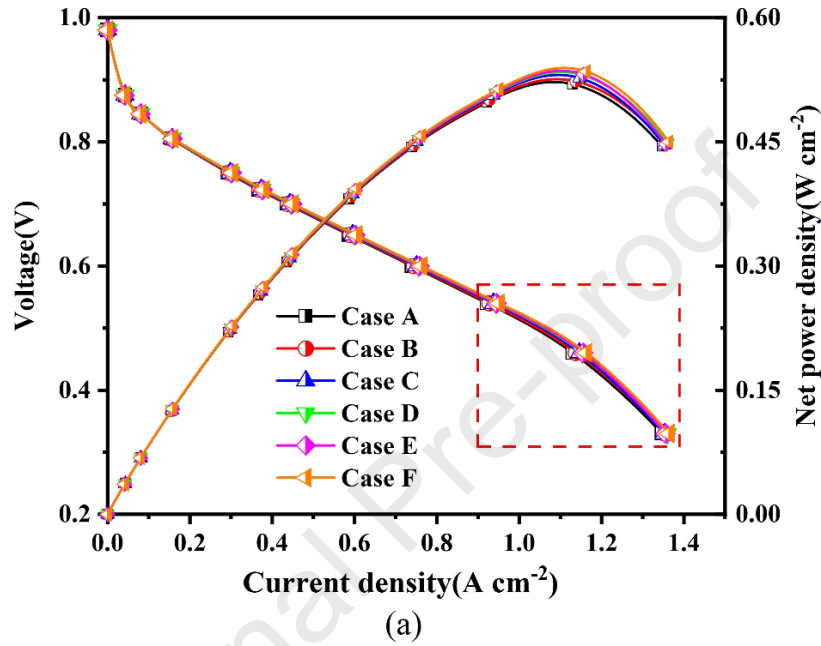


Figure 7 (a): Polarization curve and net power density curve;(b): Local amplification of Case A to Case F at low working voltage.

The temperature distribution on the central section of MEM and the liquid water saturation on the central section of cathode CL have been indicated in Fig. 8 with the operating voltage of 0.33V. Fig. 8(a) illustrates that the higher the coolant velocity, the lower the temperature on the MEM under the same cooling runner pattern. Moreover, the MEM temperature of the wave CC is slightly lower than the straight CC, indicating that the cooling effect of the wave CC is better. The liquid water saturation distribution of the cathode CL is shown in Fig. 8(b). The cathode CL liquid water saturation of the wave CC is slightly higher than the straight CC at the same flow velocity. Liquid water is generated more quickly in cathode CL at a higher current density. Due to the severe influence of temperature on the evaporation of liquid water, the higher the temperature, the faster the liquid water evaporates. However, when the temperature on MEM is low, the evaporation rate of liquid water in cathode CL and GDL is slower, which leads to liquid water accumulation.

Fig. 9(a) shows the flow profiles of CC in the y-direction central section. Overall, the average velocity of the wave CC is slightly higher than that of the straight CC, which is especially obvious close to the walls. This contributes to the explanation of the superior cooling performance of the Wave CC. Fig. 9 (b) shows the vector streamline diagram of CC in the y-direction central section. Obviously, wave CC achieves higher velocity and continuously collides with the channel walls. The velocity of straight CC is slower and parallel to the channel wall, which is not conducive to heat exchange. Therefore, the heat transfer capacity of straight CC is inferior to that of wave CC.

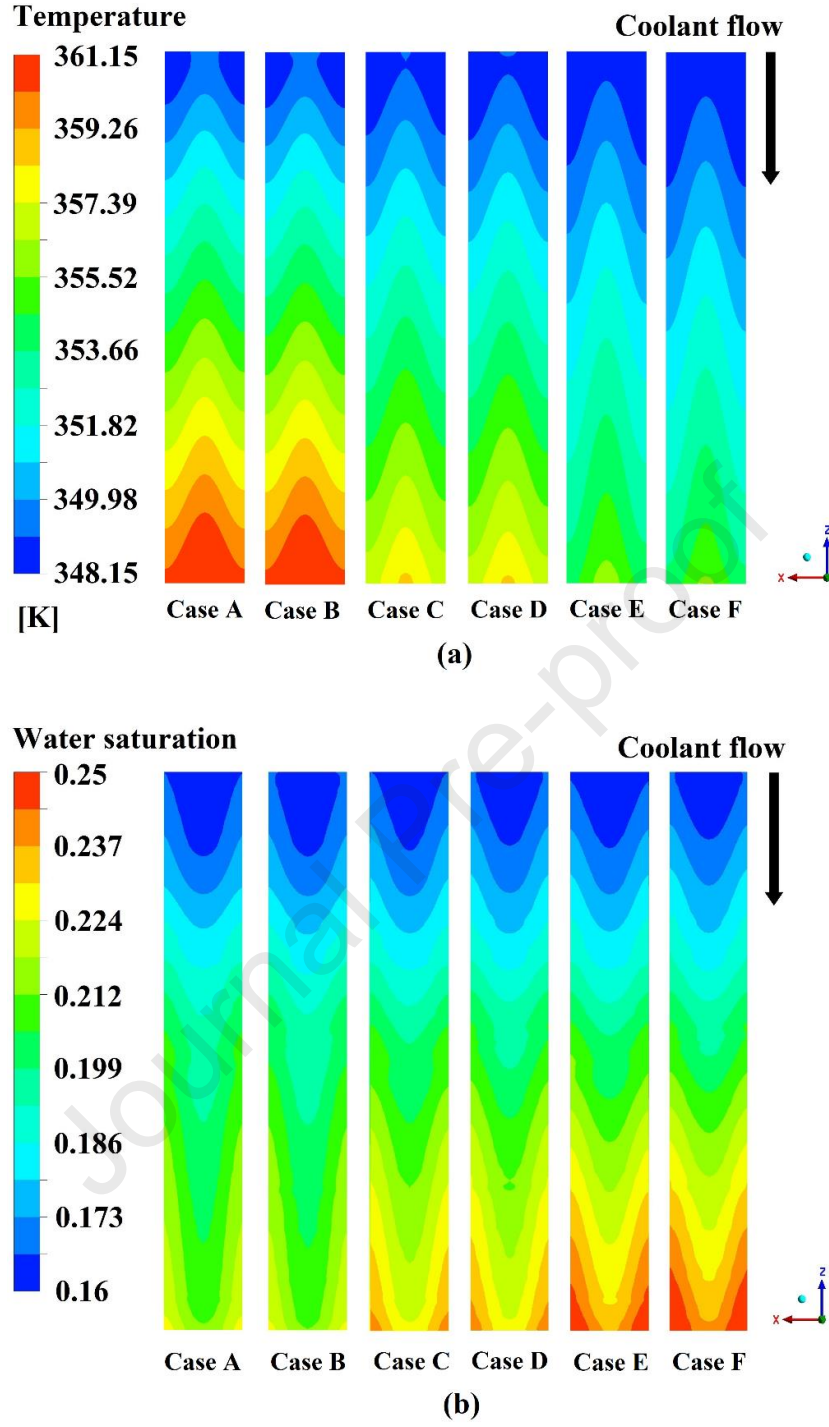


Figure 8 At 0.33V, (a): Temperature distribution on the central section of MEM (b):

Water saturation distribution on the central section of Cathode CL

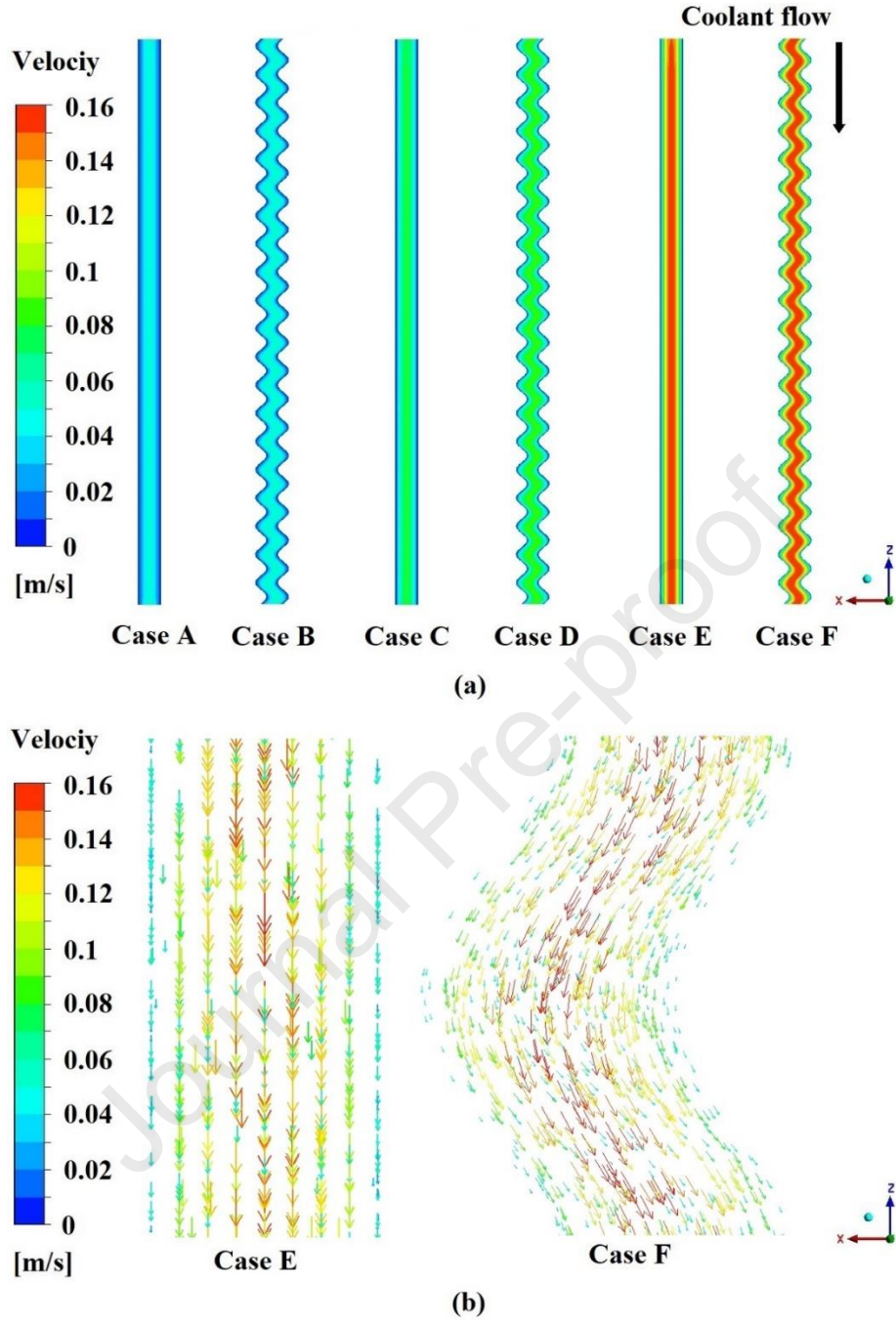


Figure 9 At 0.33V, (a): Flow profiles of CC in y-direction central section (b): Vector streamline diagram of a half period in wave CC.

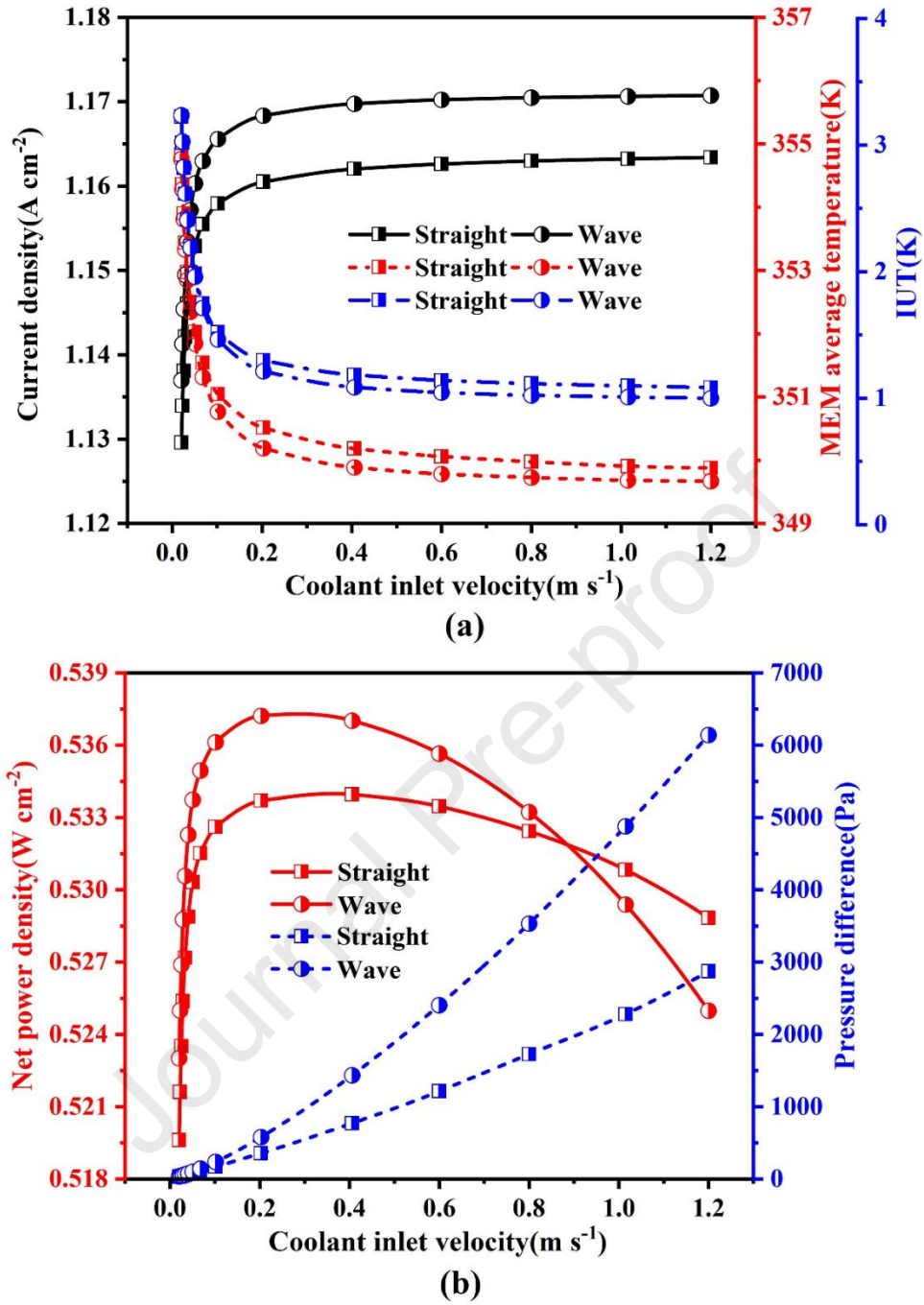


Figure 10 At 0.46V, with 343.15K coolant inlet temperature, under different coolant velocities, (a): Current density curves, MEM average temperature curves and IUT curves; (b): Net power density and pressure difference

To further investigate the optimal performance, the current density, MEM average temperature, and IUT of MEM at different coolant velocities are shown in Fig. 10(a). The figure shows that the current density increases with the increase of coolant velocity,

and the growth trend slows down with the increase of coolant velocity. When the coolant velocity is greater than 0.2 m/s, the coolant velocity has little effect on the current density. Furthermore, a very similar decreasing trend is observed in the average temperature and IUT of the MEM with the increase of coolant velocity. This indicates that there is a limitation to the cooling effect on MEM by increasing the coolant velocity at the same coolant temperature.

Fig. 10(b) manifests the net power density and pressure difference at different coolant velocities at 0.46V. The net power density increased rapidly with the coolant velocity increased from 0.02 m/s to 0.2 m/s. At low coolant velocity, the net power density curve's trend is the same as the current density curve due to the lower pressure difference. Meanwhile, the pressure difference of the straight CC is higher than 1000 Pa with a coolant velocity higher than 0.6 m/s, whereas the pressure difference of the wave CC is already higher than 1000 Pa when the coolant velocity is higher than 0.4 m/s. The huge pressure difference causes significant parasitic power, resulting in a decrease in net power density. The PEMFC with wave CC achieves a peak net power density of 0.537 W/cm^2 under the coolant velocity of approximately 0.2 m/s, while the PEMFC with straight CC achieves a peak net power density of 0.534 W/cm^2 at the coolant velocity of 0.4 m/s. After reaching the peak power density, the net power densities of wave CC and straight CC decrease with increasing coolant velocity in different trends. Due to the growth rate of pressure difference in wave CC is much faster than that in straight CC, the net power density of wave CC decreases more rapidly than that of straight CC. Wave CC achieves a higher net power density when the coolant

velocity is approximately below 0.9 m/s. And the net power density of straight CC exceeds that of wave CC when the coolant velocity exceeds 0.9m/s. Although increasing the coolant velocity can improve the cooling effect of PEMFC and thereby enhance its performance, it inevitably leads to an increase in parasitic power, thereby reducing the output power of the PEMFC system.

4.3 Effect of coolant flow direction

To investigate how coolant flow direction affects PEMFC performance, two opposing coolant flow directions, one for the same as hydrogen and the other for the same as oxygen were examined, respectively. The pressure difference is virtually independent of the coolant flow direction at the same CC and coolant velocity, hence the effect of coolant flow direction on parasitic power can be neglected. Therefore, analyzing the current density is sufficient to explore the effect of coolant flow direction on PEMFC performance. Fig. 11(a) manifests the current density of straight CC and wave CC under different coolant directions and coolant temperature differences. It is found that the coolant direction, the same as H₂, has better performance at the coolant temperature difference higher than 6K. On the contrary, the coolant direction, the same as O₂, has better performance at the coolant temperature difference less than 6K. It means that the temperature difference of 6K is a critical value. From Fig. 11(b), the influence of coolant direction on the average temperature of MEM for the same CC decreases as the coolant temperature difference decreases. Furthermore, the PEMFC achieved better performance at the temperature of MEM close to 350K. Fig. 11(b) also shows the MEM average temperature and IUT of straight CC and wave CC for different coolant flow

directions and temperature differences. The same coolant flow direction as H_2 has a lower average MEM temperature. However, the same coolant flow direction as O_2 has a lower IUT on MEM.

Fig. 12 shows the MEM temperature distribution of different coolant temperature differences and coolant flow directions. Fig.12 shows that the temperature distribution on MEM is more uniform and is closer to 350K with the same coolant direction as O_2 when the temperature difference between the coolant is less than 6K. When the direction of coolant is the same as H_2 , the temperature on the cathode inlet is higher due to the stoichiometry ratio of H_2 being higher than O_2 in this study. In addition, the flow direction of H_2 and O_2 is opposite, with more H_2 flowing directly to the end of the anode channel and reacting with the O_2 just entering the cathode channel. Little O_2 flows to the end of the cathode channel for reaction. Therefore, with the coolant flowing in the same direction as H_2 , the anode inlet is over-cooled, but the anode outlet is not thoroughly cooled. Although the average temperature on MEM is relatively low, the temperature difference on MEM is significant, and the IUT is also large. Conversely, when the coolant flow direction is the same as O_2 , the cathode inlet side and outlet side are thoroughly cooled, leading to a relatively small temperature difference on the MEM and a relatively small value of IUT.

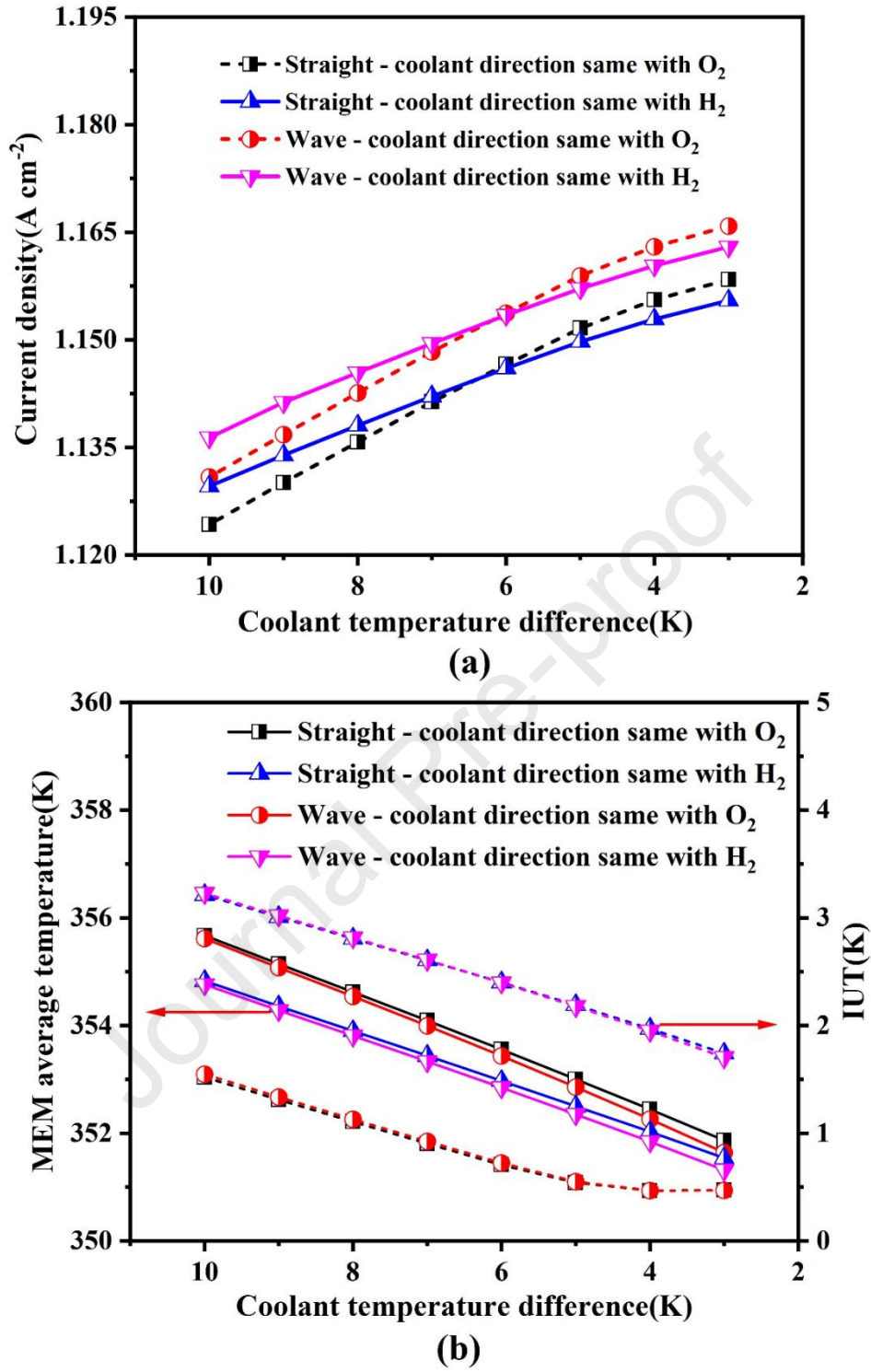


Figure 11 At different coolant temperature difference the effect of cooling directions

on (a): Current density; (b): MEM average temperature and IUT

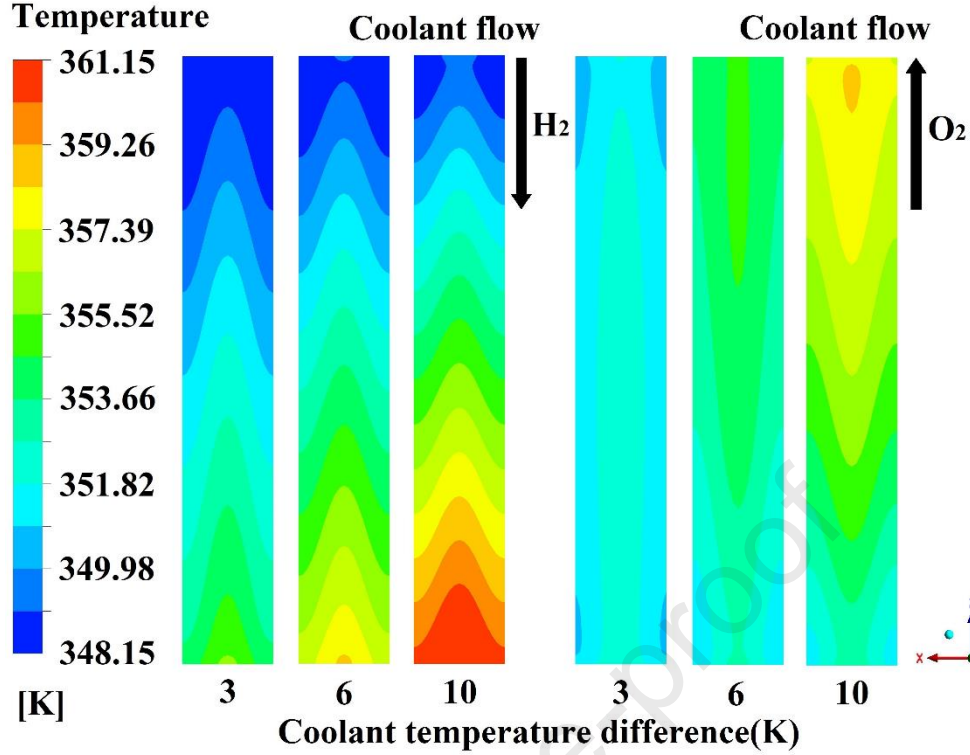


Figure 12 MEM temperature distribution at different coolant temperature difference and coolant flow direction

4.4 Nusselt number

The Nusselt number can compare the heat transfer performance of the wave CC and the straight CC. Nusselt number represents the intensity of convective heat transfer as follows [60] :

$$Nu = \frac{h_x D_h}{k} = \frac{-D_h \cdot \partial T / \partial y|_{y=0}}{(T_{in} - T_w)} \quad (32)$$

Where k is the thermal conductivity, $D_h = 0.00089\text{m}$ is the hydraulic diameter, h_x is the convective heat transfer coefficient, T_{in} is the volume average temperature on the cross-section of CC, T_w is the wall temperature of CC.

Fig. 13(a) shows that the surface Nusselt number on the centerline of the interface between the CC and the BP in the z-axis direction with a contours plot at 0.46 V, and

the flow direction of the coolant is the same as H_2 . For the straight CC, such as Case A, Case C, and Case E, the surface Nusselt number exhibits power-law reduction and asymptotically approaches a value of 0.275, 0.537, and 1.093, respectively [60]. While for the wave CC, such as Case B, Case D, and Case F, the surface Nusselt number is slightly higher than that of the straight CC and gradually oscillates down with a similar trend to the straight CC. From the contour plot in Fig. 13(a), the Nusselt number at the inlet of the wave CC is greater than the straight CC, especially for higher coolant velocity (Case E and Case F). In addition, it is evident that the Nusselt number increases with the increase of coolant velocity. Fig. 13(b) shows the average Nusselt number at the interface between the cathode CC and the BP wall from Case A to Case F. It is observed that at a lower coolant velocity (Case A and Case B), the average Nusselt number for the wave CC is 0.753, which is 5.46% higher than the 0.714 for the straight CC. At a middle coolant velocity (Case C and Case D), the average Nusselt number for the wave CC is 1.136, which is 8.92% higher than the 1.043 for the straight CC. Furthermore, at a higher coolant velocity (Case E and Case F), the average Nusselt number for the wave CC is 1.954, which is 18.71% higher than the 1.646 for the straight CC.

To summarize, the surface Nusselt number of the wavy CC is higher than that of the straight CC. When the coolant velocity is increased, the average Nusselt number of the Wave CC can increase more than that of the Straight CC, which means wavy CC has a much stronger convection heat transfer performance than straight CC.

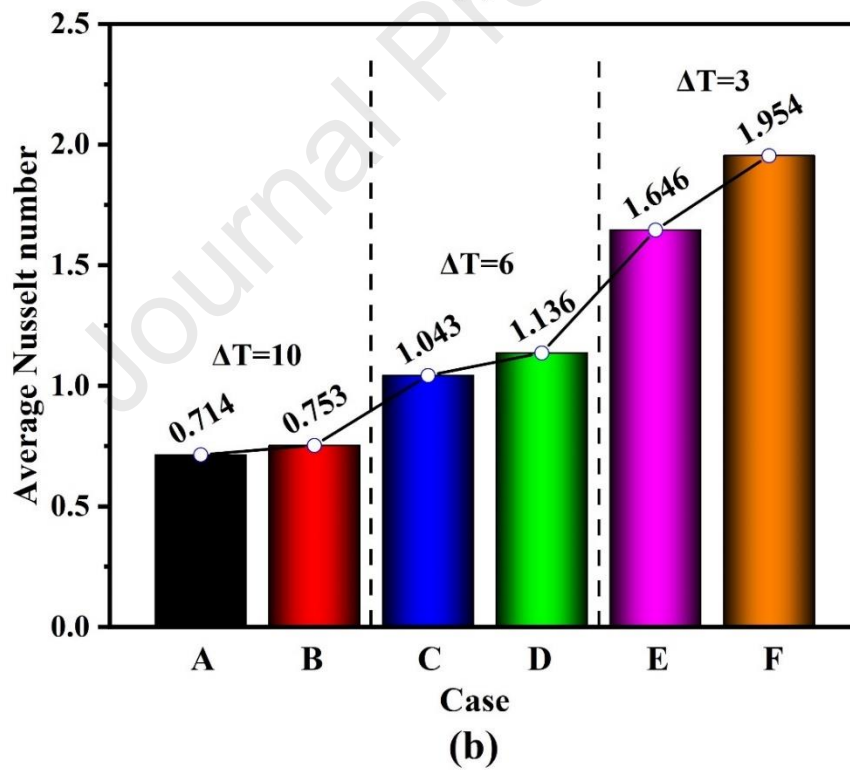
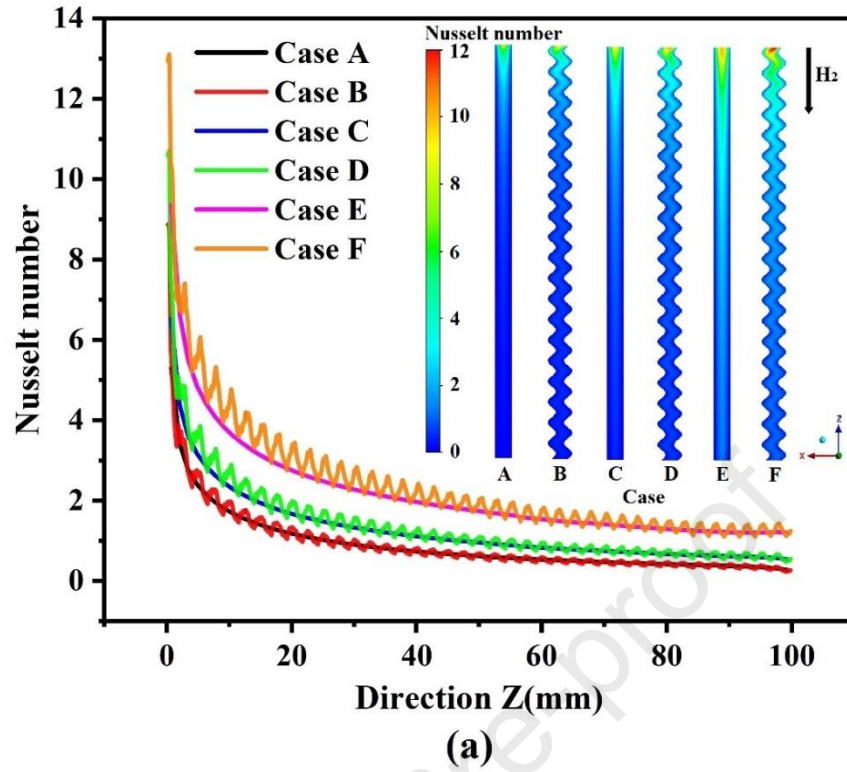


Figure 13 (a): Surface Nusselt number on the centerline of z-axis with contours plot;

(b): Average surface Nusselt number of whole CC surface

5. Conclusion

In this study, three-dimensional multiphase PEMFC electrochemical models integrating straight CC and wave CC were established to investigate the heat transfer performance. The causes affecting heat transfer are analyzed in detail, and various evaluation indicators were used to evaluate heat transfer performance. The main conclusions are as follows:

1. With the same coolant velocity, coolant direction and operating voltage, the current density of the PEMFC and the temperature distribution on the MEM is significantly influenced by the coolant inlet temperature. Additionally, the coolant inlet temperature is linearly correlated with the average temperature of the MEM. While the temperature of MEM directly determines the performance of PEMFC. When the temperature distribution on the MEM is very close, the smaller the value of IUT, the better the performance of PEMFC.
2. The liquid water distribution on CL is directly affected by the MEM temperature distribution. At lower operating voltage, too low MEM temperature can make it difficult to remove liquid water from the CL. Even flooding occurs in serious cases, which blocks gas transfer. The flooding can cause the reaction gas not easily combined with the catalyst, increase the mass transfer resistance, reduce the output power, and cause a serious impact on the PEMFC life and performance.
3. The performance of PEMFC with wave CC is slightly better than that of straight CC. Increasing the coolant velocity at a low coolant velocity (less than 0.2 m/s) can significantly improve the current density. As the coolant velocity increases

from 0.02 m/s to 0.2 m/s, the current density increases with straight and wave CC. Straight CC and wave CC reach peak net power density at 0.4m/s and 0.2m/s, respectively. However, as the coolant velocity increases from 0.2 m/s to 1.2 m/s, the current density increases very slowly due to the considerable pressure difference, and the net power densities of the straight CC and wave CC decrease by 0.92%% and 2.27%, respectively.

4. The average temperature on MEM with the same direction of coolant as H₂ is lower than that with the same direction of coolant as O₂. At higher coolant velocity, PEMFC has better performance and uniformity of temperature distribution on MEM (IUT lower than 1K) at the coolant flow direction is the same as O₂.
5. The surface Nusselt number of wave CC is greater than straight CC under the same working conditions. With the temperature difference between the coolant inlet and outlet of 10K, 6K, and 3K, the surface Nusselt number of wave CC is 5.46%, 8.92%, and 18.71% higher than the straight CC, respectively.

Acknowledgement

The authors would like to acknowledge the financial support from National Natural Science Foundation of China (No.52176200).

References:

- [1] K. Meng, H. Zhou, B. Chen, et al. Dynamic current cycles effect on the degradation characteristic of a H₂/O₂ proton exchange membrane fuel cell. *Energy*, 2021, 224: 120168.
- [2] B. Chen, H. Zhou, S. He, et al. Numerical simulation on purge strategy of proton

exchange membrane fuel cell with dead-ended anode. *Energy*, 2021, 234: 121265.

[3] K. Jiao, J. Xuan, Q. Du, et al. Designing the next generation of proton-exchange membrane fuel cells. *Nature*, 2021, 595(7867): 361-369.

[4] B. Chen, Q. Liu, C. Zhang, et al. Numerical study on water transfer characteristics under joint effect of placement orientation and flow channel size for PEMFC with dead-ended anode. *Energy*, 2022, 254: 124365.

[5] H. Huang, X. Li, S. Li, et al. Evaluating the effect of refined flow channels in a developed biomimetic flow field on PEMFC performance. *Energy*, 2023, 266: 126442.

[6] Y. Zhou, B. Chen, W. Chen, et al. A novel opposite sinusoidal wave flow channel for performance enhancement of proton exchange membrane fuel cell. *Energy*, 2022, 261: 125383.

[7] B. Tanç, H. T. Arat, E. Baltacıoğlu, et al. Overview of the next quarter century vision of hydrogen fuel cell electric vehicles. *International Journal of Hydrogen Energy*, 2019, 44(20): 10120-10128.

[8] P. Ahmadi, M. Raeesi, S. Changizian, et al. Lifecycle assessment of diesel, diesel-electric and hydrogen fuel cell transit buses with fuel cell degradation and battery aging using machine learning techniques. *Energy*, 2022, 259: 125003.

[9] Z. Huang, Q. Jian. Cooling efficiency optimization on air-cooling PEMFC stack with thin vapor chambers. *Applied Thermal Engineering*, 2022, 217: 119238.

[10] A. Mahdavi, A. A. Ranjbar, M. Gorji, et al. Numerical simulation based design for an innovative PEMFC cooling flow field with metallic bipolar plates. *Applied Energy*, 2018, 228: 656-666.

- [11] H. Shen, Y. Huang, H. Kang, et al. Effect of the cooling water flow direction on the performance of PEMFCs. *International Journal of Heat and Mass Transfer*, 2022, 189: 122303.
- [12] H. Pourrahmani, M. Siavashi, M. Moghimi, et al. Design optimization and thermal management of the PEMFC using artificial neural networks. *Energy*, 2019, 182: 443-459.
- [13] J. Xu, C. Zhang, Z. Wan, et al. Progress and perspectives of integrated thermal management systems in PEM fuel cell vehicles: A review. *Renewable and Sustainable Energy Reviews*, 2022, 155: 111908.
- [14] E. Ogungbemi, O. Ijaodola, F. N. Khatib, et al. Fuel cell membranes – Pros and cons. *Energy*, 2019, 172: 155-172.
- [15] Z. Song, Y. Pan, H. Chen, et al. Effects of temperature on the performance of fuel cell hybrid electric vehicles: A review. *Applied Energy*, 2021, 302: 117572.
- [16] Q. Li, C. Wang, C. Wang, et al. Comparison of organic coolants for boiling cooling of proton exchange membrane fuel cell. *Energy*, 2023, 266: 126342.
- [17] T. F. Cao, H. Lin, L. Chen, et al. Numerical investigation of the coupled water and thermal management in PEM fuel cell. *Applied Energy*, 2013, 112: 1115-1125.
- [18] M. Ramezanizadeh, M. Alhuyi Nazari, M. Hossein Ahmadi, et al. A review on the approaches applied for cooling fuel cells. *International Journal of Heat and Mass Transfer*, 2019, 139: 517-525.
- [19] D. Qiu, L. Peng, J. Tang, et al. Numerical analysis of air-cooled proton exchange membrane fuel cells with various cathode flow channels. *Energy*, 2020, 198: 117334.

- [20] G. Zhang, S. G. Kandlikar. A critical review of cooling techniques in proton exchange membrane fuel cell stacks. *International Journal of Hydrogen Energy*, 2012, 37(3): 2412-2429.
- [21] M. V. Oro, E. Bazzo. Flat heat pipes for potential application in fuel cell cooling. *Applied Thermal Engineering*, 2015, 90: 848-857.
- [22] W. Huang, Q. Jian, S. Feng, et al. A hybrid optimization strategy of electrical efficiency about cooling PEMFC combined with ultra-thin vapor chambers. *Energy Conversion and Management*, 2022, 254: 115301.
- [23] Z. Huang, Q. Jian, L. Luo, et al. Rapid thermal response and sensitivity analysis of proton exchange membrane fuel cell stack with ultra-thin vapor chambers. *Applied Thermal Engineering*, 2021, 199: 117526.
- [24] W. W. Yuan, K. Ou, Y.-B. Kim. Thermal management for an air coolant system of a proton exchange membrane fuel cell using heat distribution optimization. *Applied Thermal Engineering*, 2020, 167: 114715.
- [25] A. Baroutaji, A. Arjunan, M. Ramadan, et al. Advancements and prospects of thermal management and waste heat recovery of PEMFC. *International Journal of Thermofluids*, 2021, 9: 100064.
- [26] M. Sajid Hossain, B. Shabani. Metal foams application to enhance cooling of open cathode polymer electrolyte membrane fuel cells. *Journal of Power Sources*, 2015, 295: 275-291.
- [27] B. D. Gould, R. Ramamurti, C. R. Osland, et al. Assessing fuel-cell coolant flow fields with numerical models and infrared thermography. *International Journal of*

Hydrogen Energy, 2014, 39(26): 14061-14070.

[28] I. Zakaria, W. a. N. W. Mohamed, A. M. I. B. Mamat, et al. Thermal Analysis of Heat Transfer Enhancement and Fluid Flow for Low Concentration of Al_2O_3 Water - Ethylene Glycol Mixture Nanofluid in a Single PEMFC Cooling Plate. Energy Procedia, 2015, 79: 259-264.

[29] R. Islam, B. Shabani, J. Andrews, et al. Experimental investigation of using ZnO nanofluids as coolants in a PEM fuel cell. International Journal of Hydrogen Energy, 2017, 42(30): 19272-19286.

[30] S. Chen, X. Wang, W. Li, et al. Experimental study on cooling performance of microencapsulated phase change suspension in a PEMFC. International Journal of Hydrogen Energy, 2017, 42(50): 30004-30012.

[31] C. Chen, C. Wang, X. Wang, et al. Study on the performance and characteristics of fuel cell coupling cathode channel with cooling channel. International Journal of Hydrogen Energy, 2021, 46(54): 27675-27686.

[32] S. M. Baek, S. H. Yu, J. H. Nam, et al. A numerical study on uniform cooling of large-scale PEMFCs with different coolant flow field designs. Applied Thermal Engineering, 2011, 31(8-9): 1427-1434.

[33] X. Chen, Q. Liu, Y. Fang, et al. Numerical study of a MIMO-shaped cooling plate in PEMFC stack for heat transfer enhancement. Energy Reports, 2021, 7: 5804-5814.

[34] Z. Yong, H. Shirong, J. Xiaohui, et al. Performance study on a large-scale proton exchange membrane fuel cell with cooling. International Journal of Hydrogen Energy, 2022, 47(18): 10381-10394.

- [35] Z. Yong, H. Shirong, J. Xiaohui, et al. Characteristics of proton exchange membrane fuel cell considering “dot matrix” gas distribution zones and waveform staggered flow field with cooling channels. *Energy Conversion and Management*, 2022, 267:115881.
- [36] E. Alizadeh, S. M. Rahgoshay, M. Rahimi-Esbo, et al. A novel cooling flow field design for polymer electrolyte membrane fuel cell stack. *International Journal of Hydrogen Energy*, 2016, 41(20): 8525-8532.
- [37] Q. Deng, Y. Liu, Y. Zhou, et al. Evaluation of cooling flow field of proton exchange membrane fuel cell based on heat transfer performance enhancement. *International Journal of Energy Research*, 2022, 46(9): 12519-12529.
- [38] E. Afshari, M. Ziaei-Rad, M. M. Dehkordi. Numerical investigation on a novel zigzag-shaped flow channel design for cooling plates of PEM fuel cells. *Journal of the Energy Institute*, 2017, 90(5): 752-763.
- [39] E. Afshari, M. Ziaei-Rad, Z. Shariati. A study on using metal foam as coolant fluid distributor in the polymer electrolyte membrane fuel cell. *International Journal of Hydrogen Energy*, 2016, 41(3): 1902-1912.
- [40] J. Song, Y. Huang, J. Zeng, et al. Design and numerical investigation of multi-channel cooling plate for proton exchange membrane fuel cell. *Energy Reports*, 2022, 8: 6058-6067.
- [41] S. H. Yu, S. Sohn, J. H. Nam, et al. Numerical study to examine the performance of multi-pass serpentine flow-fields for cooling plates in polymer electrolyte membrane fuel cells. *Journal of Power Sources*, 2009, 194(2): 697-703.

- [42] Y. Vazifeshenas, K. Sedighi, M. Shakeri. Heat transfer in PEM cooling flow field with high porosity metal foam insert. *Applied Thermal Engineering*, 2019, 147: 81-89.
- [43] S. Li, B. Sundén. Numerical analysis on thermal performance of cooling plates with wavy channels in PEM fuel cells[J]. *International Journal of Numerical Methods for Heat & Fluid Flow*, 2018, 28(7): 1684-1697.
- [44] S. Li, B. Sundén. Numerical study on thermal performance of non-uniform flow channel designs for cooling plates of PEM fuel cells[J]. *Numerical Heat Transfer, Part A: Applications*, 2018, 74(1): 917-930.
- [45] S. M. Rahgoshay, A. A. Ranjbar, A. Ramiar, et al. Thermal investigation of a PEM fuel cell with cooling flow field. *Energy*, 2017, 134: 61-73.
- [46] A. P. Sasmito, J. C. Kurnia, A. S. Mujumdar. Numerical evaluation of various gas and coolant channel designs for high performance liquid-cooled proton exchange membrane fuel cell stacks. *Energy*, 2012, 44(1): 278-291.
- [47] Ž. Penga, G. Radica, F. Barbir, et al. Coolant induced variable temperature flow field for improved performance of proton exchange membrane fuel cells. *International Journal of Hydrogen Energy*, 2019, 44(20): 10102-10119.
- [48] X. Liu, Z. Zhou, M. Bai, et al. Three-dimensional simulations for counter - flow proton exchange membrane fuel cells with thin catalyst - coated membrane cooled by liquid water. *International Journal of Energy Research*, 2022, 46(9): 11778-11801.
- [49] S. A. Atyabi, E. Afshari, C. Udemu. Comparison of active and passive cooling of proton exchange membrane fuel cell using a multiphase model. *Energy Conversion and Management*, 2022, 268: 115970.

- [50] S. A. Atyabi, E. Afshari, E. Zohravi, et al. Three-dimensional simulation of different flow fields of proton exchange membrane fuel cell using a multi-phase coupled model with cooling channel. *Energy*, 2021, 234: 121247.
- [51] S. A. Atyabi, E. Afshari. Three-dimensional multiphase model of proton exchange membrane fuel cell with honeycomb flow field at the cathode side. *Journal of Cleaner Production*, 2019, 214: 738-748.
- [52] S. A. Atyabi, E. Afshari, N. Shakarami. Three-dimensional multiphase modeling of the performance of an open-cathode PEM fuel cell with additional cooling channels. *Energy*, 2023, 263: 125507.
- [53] M. Ghasemi, A. Ramiar, A. A. Ranjbar, et al. A numerical study on thermal analysis and cooling flow fields effect on PEMFC performance. *International Journal of Hydrogen Energy*, 2017, 42(38): 24319-24337.
- [54] H. Liu, G. Zhang, D. Li, et al. Three-dimensional multi-phase simulation of cooling patterns for proton exchange membrane fuel cell based on a modified Bruggeman equation. *Applied Thermal Engineering*, 2020, 174: 115313.
- [55] J. Wang, S. Wang, Y. Zhu, et al. Effect of cooling surface temperature difference on the performance of high-temperature PEMFCs, *International Journal of Hydrogen Energy*, 2023, 48(44):16813-16828.
- [56] L. Fan, G. Zhang, K. Jiao. Characteristics of PEMFC operating at high current density with low external humidification. *Energy Conversion and Management*, 2017, 150: 763-774.
- [57] K. H. Kim, K.-Y. Lee, S.-Y. Lee, et al. The effects of relative humidity on the

performances of PEMFC MEAs with various Nafion® ionomer contents. International Journal of Hydrogen Energy, 2010, 35(23): 13104-13110.

[58] G. Zhang, J. Wu, Y. Wang, et al. Investigation of current density spatial distribution in PEM fuel cells using a comprehensively validated multi-phase non-isothermal model. International Journal of Heat and Mass Transfer, 2020, 150: 119294.

[59] S. Yu, D. Jung. Thermal management strategy for a proton exchange membrane fuel cell system with a large active cell area. Renewable Energy, 2008, 33(12): 2540-2548.

[60] J. K. Kuo, C. O.-K. Chen. Evaluating the enhanced performance of a novel wave-like form gas flow channel in the PEMFC using the field synergy principle. Journal of Power Sources, 2006, 162(2): 1122-1129.

Abbreviation

<i>PEMFC</i>	<i>Proton exchange membrane fuel cell</i>
<i>PEMFCVs</i>	<i>Proton exchange membrane fuel cell vehicles</i>
<i>CFD</i>	<i>Computation fluid dynamics</i>
<i>MIMO</i>	<i>Multi-input and multi-output</i>
<i>IUT</i>	<i>Index of temperature uniformity</i>
<i>BP</i>	<i>Bipolar plate</i>
<i>CC</i>	<i>Cooling Channel</i>
<i>GDL</i>	<i>Gas diffusion layer</i>
<i>CL</i>	<i>Catalyst layer</i>
<i>MEM</i>	<i>Membrane</i>

Nomenclature

δ	<i>Thickness, μm</i>
W	<i>Width, mm</i>
H	<i>Height, mm</i>
L	<i>Length, mm</i>
K	<i>Intrinsic permeability, m^2</i>
k	<i>Thermal conductivity, $\text{W m}^{-1} \text{K}^{-1}$</i>
ω	<i>Ionomer volume fraction</i>
ρ	<i>Density, kg m^{-3}</i>
\vec{u}	<i>Velocity vector, m s^{-1}</i>
S	<i>Source term, ($\text{kg m}^{-3} \text{s}^{-1}$ or $\text{mol m}^{-3} \text{s}^{-1}$)</i>
ε	<i>Porosity</i>
P	<i>Pressure, Pa</i>
μ	<i>Dynamic viscosity of water, $\text{kg m}^{-1} \text{s}^{-1}$</i>
Y	<i>Gas species mass fraction</i>
D	<i>Diffusion coefficient, $\text{m}^2 \text{s}^{-1}$</i>
F	<i>Faraday constant, C mol^{-1}</i>
I_{ion}	<i>Ionic current density, A m^{-2}</i>
λ	<i>Membrane water content</i>
EW	<i>Equivalent mass of membrane, kg mol^{-1}</i>
C_p	<i>Constant pressure specific heat, $\text{J K}^{-1} \text{mol}^{-1}$</i>
s	<i>Liquid water saturation</i>

k_e^{eff}	<i>Effective thermal conductivity, $W m^{-1} K^{-1}$</i>
T	<i>Temperature, K</i>
k_l	<i>Liquid phase relative permeability</i>
k_g	<i>Gas phase relative permeability</i>
P_c	<i>Capillary pressure, Pa</i>
σ	<i>Surface tension coefficient, $N m^{-1}$</i>
θ	<i>Contact angle, $^{\circ}$</i>
κ	<i>Electronic conductivity, $S m^{-1}$</i>
φ	<i>Potential, V</i>
J	<i>Exchange current density, $A m^{-3}$</i>
α	<i>Charge transfer coefficient</i>
η	<i>Overpotential, V</i>
R	<i>Universal gas constant, $J mol^{-1} K^{-1}$</i>
E_{rev}	<i>Reversible voltage, V</i>
ΔS	<i>Entropy change, $J mol^{-1} K^{-1}$</i>
γ_{cond}	<i>Condensation rate, s^{-1}</i>
γ_{evap}	<i>Evaporation rate, s^{-1}</i>
h	<i>Latent heat coefficient, $J mol^{-1}$</i>
C	<i>Molar concentration, $mol m^{-3}$</i>
\dot{m}	<i>Mass flow rate, $kg s^{-1}$</i>
ξ	<i>Stoichiometric ratio</i>
A	<i>Active area, cm^2</i>

RH	<i>Relative humidity</i>
Q_c	<i>Coolant flow, $m^3 s^{-1}$</i>
q	<i>Exothermic power density, $W cm^{-2}$</i>
n	<i>Amount of single cell</i>
ΔT	<i>Coolant temperature difference between inlet and outlet, K</i>
V_{in}	<i>Coolant inlet velocity, $m s^{-1}$</i>
A_{in}	<i>Coolant inlet area, m^2</i>
T_{avg}	<i>Average temperature</i>
P_{net}	<i>Net power density, $W cm^{-2}$</i>
P_{gross}	<i>Total output power, $W cm^{-2}$</i>
P_{para}	<i>Parasitic power, $W cm^{-2}$</i>
V_{cell}	<i>Cell voltage, V</i>
j	<i>Average current density, $A cm^{-2}$</i>
η_{pump}	<i>Efficiency of pump</i>
Nu	<i>Nussle number</i>
h_x	<i>Convective heat transfer coefficient, $W m^{-2} K^{-1}$</i>
D_h	<i>Hydraulic diameter, m</i>

Numerical study on heat transfer characteristics and performance evaluation of PEMFC based on multiphase electrochemical model coupled with cooling channel

- > A three-dimensional multi-phase PEMFC electrochemical model coupled with cooling channel is developed
- > IUT, net power and Nusselt number are applied to evaluate the heat transfer performance
- > The effect of coolant flow direction on performance depends on the flow velocity
- > Performance of PEMFC with wave cooling channel is slightly better than that of straight cooling channel

Declaration of interests

☒ The authors declare that they have no known competing financial interests or personal relationships that could have appeared to influence the work reported in this paper.

☐ The authors declare the following financial interests/personal relationships which may be considered as potential competing interests: